ALMA MATER STUDIORUM – UNIVERSITÀ DI BOLOGNA

SCUOLA DI INGEGNERIA E ARCHITETTURA

DIN

CORSO DI LAUREA MAGISTRALE IN INGEGNERIA ENERGETICA

TESI DI LAUREA MAGISTRALE

in

ELECTROCHEMICAL ENERGY STORAGE AND CONVERSION

Cobalt-free cathode for high voltage lithium-ion batteries

Candidato:

Andrea Trebbi

Relatore:

Prof.ssa Francesca Soavi

Correlatori:

Dr. Daniele Marchese

Dr. Antunes Staffolani

Anno Accademico 2022/23

Summary

Abstract

The constant growth in the demand of clean energy is driving the world towards an electrification of many sectors, such as transportation and building, and towards renewable technologies for a sustainable energy production and use. For this reason, the energy storage systems will become always more important to cover the fluctuations of the energetic demand, going to compensate the non-linearity of the renewable sources. Among the types of energy storage systems, batteries, thanks to their versatility, are the most considered. In particular, the lithium-ion batteries are the most promising, both for grid-energy storage and distribution and for the utilization in electric vehicles. However, more research and technological development is needed, not only for increasing their energy density and safety, but also for decreasing the production cost and environmental impact, and for their end-of-life management, since critical materials and components with high environmental hazard are also used.

This work has been carried out under a collaborative project set between MIDAC S.p.A., partner of the IPCEI/012/00B2 program and GISEL – INSTM (Research unit: University of Bologna), and within the PNRR Project CNMS-Spoke 13-MOST.

The purpose of this thesis is the formulation of Cobalt-free, high voltage cathodes ($LiNi_{0.5}Mn_{1.5}O_4$, LMNO) for lithium-ion batteries. The electrodes featured a commercial LMNO powder and were formulated by blending this active material with carbon conductive additive and different binders, and by modifying the mass ratios of the components. The electrochemical characterization was performed by using the benchmark electrolyte used in today lithium-ion batteries, i.e., a solution of Lithium hexafluorophosphate dissolved in mixture of ethylene carbonate – dimethyl carbonate. This study provided a benchmark to MIDAC to compare the performance of the electrodes that they are developing by a recycling approach from spent batteries.

1. Introduction

Energy transition and climate changes are two of the greatest and more urgent challenges that our society must face in the XXI century. Meanwhile our dependence on fossil fuels keeps threatening the health of our planet, global warming and climate changes are causing serious damages at natural and human systems.

One of the greatest issues coming from the usage of on fossil fuels is represented by the emission of greenhouse gases (GHG) in the atmosphere, especially carbon dioxide and aqueous vapour. These greenhouse gases, as well known, keep the heat inside the atmosphere, causing an increase in the global temperature, which by consequence causes a series of climate changes.

In the last decades, indeed, the greenhouse gases emissions have significantly increased globally, as depicted in Figure 1. This is due to the massive utilization of fossil fuels for the energy production, for industrial processes and for transportations. As result, according to the IPCC report [1], the medium global temperature is increased of ca. 1.1°C compared to pre-industrial levels, from 1850 to 1900. Indeed, the global temperature increase has significant consequences on our planet, such as the warming of the oceans, the rise in sea levels, the decrease in snow cover, the increase in the frequency and intensity of extreme climatic events such as cyclones, floods, droughts and fires, and the alteration of natural ecosystems. [1]

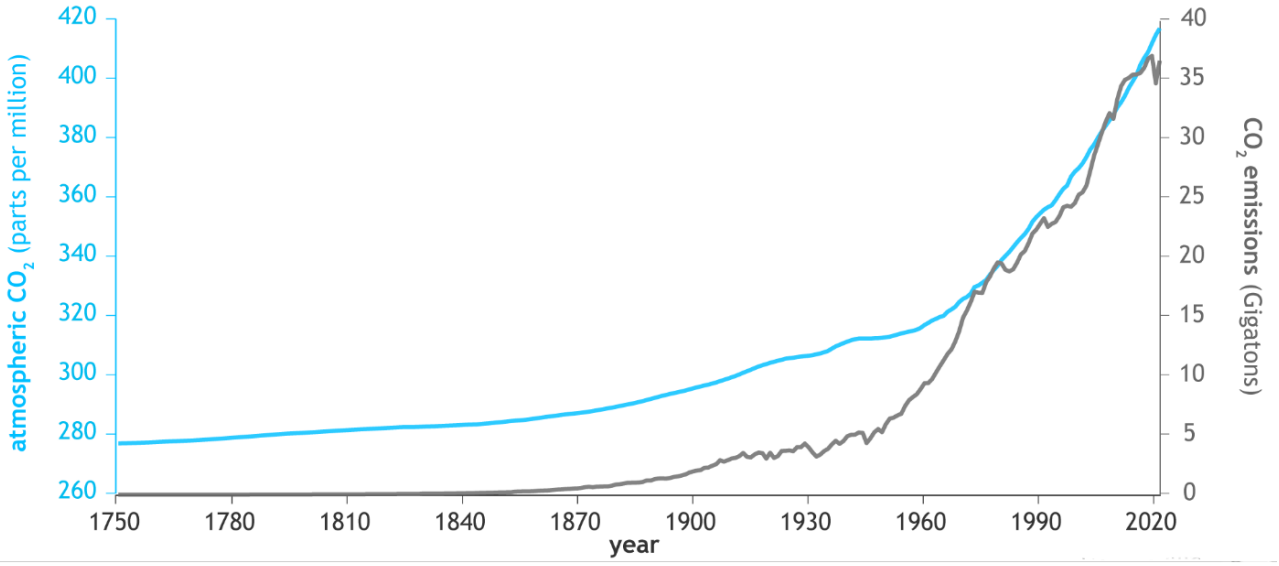

Figure 1 - Atmospheric carbon dioxide amounts and annual emissions (1750 – 2021). [2]

The urgent need for the reduction of greenhouse gases emissions was internationally recognized since the signature of the "Paris Agreement" in 2015, through which each signatory state committed to adopt green policies to limit the increase in global average temperature to below 2°C compared to pre-industrial levels, and possibly to 1.5°C. [3]

Figure 2 shows the forecast of the CO_2 emissions in which are represented three different future scenarios, strongly dependent on the policies of each state. For example, "New Momentum" scenario (green line) is the future trend of CO_2 emissions which takes into account just the progressing of the global energy system. While other trends, explore how different socio-political actions might lead to a massive reduction in carbon emissions. They are conditioned by significant climate policies to support energy efficiency as well as a shift in societal behaviour of people. The ideal aim is to reach net-zero emissions in 2050.

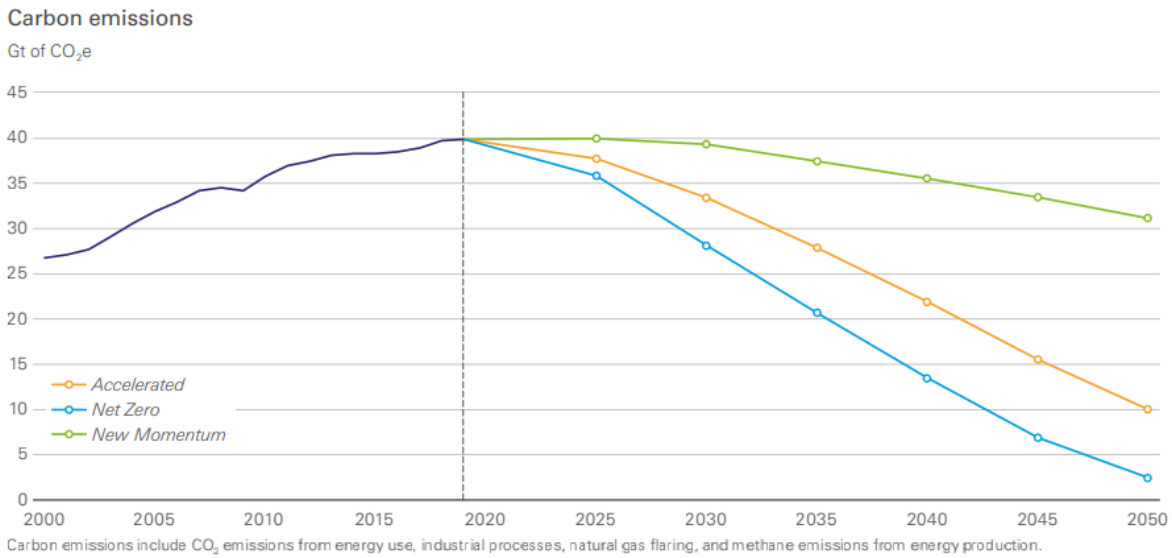

Figure 2 - Carbon emissions future trend. [4]

As highlighted by the study of "Our World in Data" [5], the most impactful sector that contributes to the production of GHG is the energy sector with almost three-quarters of emissions; almost one-fifth from agriculture and land use and the remaining 8% from industry and waste, as depicted in Figure 3. It is therefore mandatory to move as fast as we can to a decarbonized energy global system, even if there are no simple solutions. Indeed, even if we could fully decarbonize our electric supply, we would also need to electrify all of our heating and road transport. It is important to note that to reach

net-zero emissions is insufficient to focus on single sector, but we need innovations across many sectors.

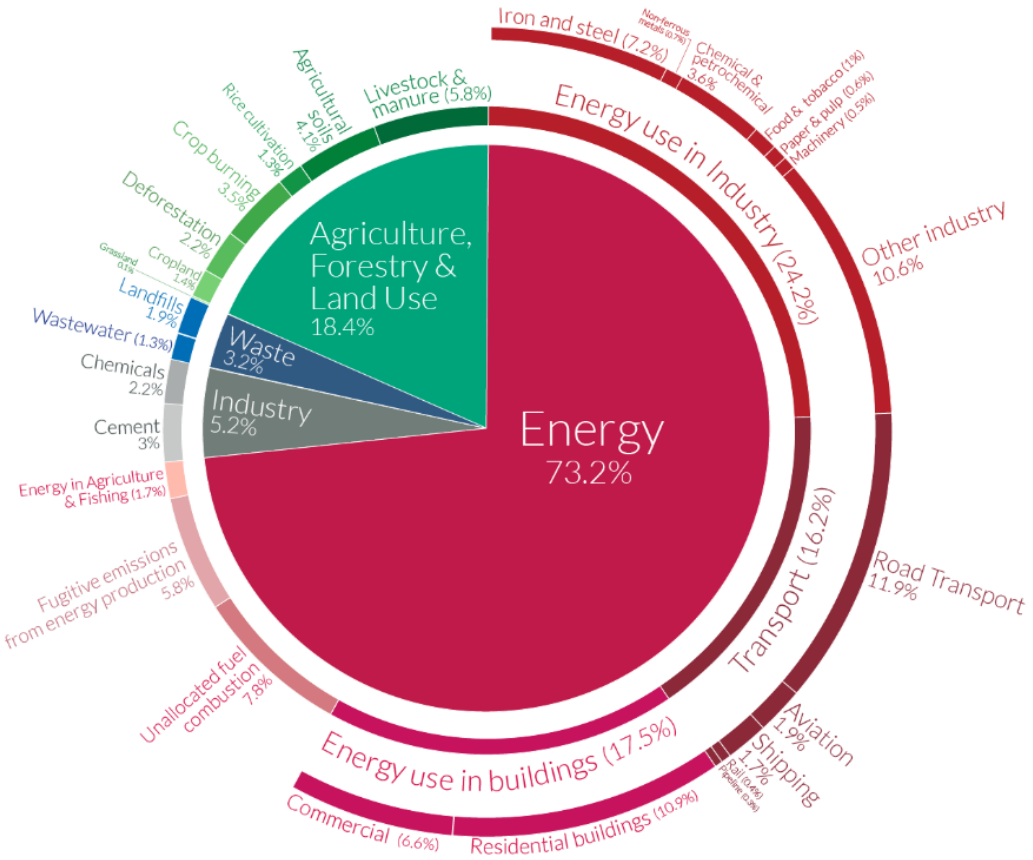

Figure 3 – Global GHG emissions by sector for the year 2016. [5]

Energy, in the form of electric energy and primary energy sources, guides the prosperity of the global economy. From 1970, the global gross domestic product has increased of ca. 4.5 times, meanwhile the consumption of primary energy has increased from 155.22 EJ in 1965 to 556.63 EJ in 2020. [6] Hence, electric energy is extremely important for the socioeconomic development. The global electric generation equal to 4114 GW in 2005 has increased to 5699 GW in 2014 and keeps increasing annually. In this regard, more than 60% was produced by fossil fuels in 2014 and it contributes to ca. 42% of the global emissions of CO_2. [6] This represents further evidence to move fast towards to the generation of energy from renewable sources.

In order to achieve climate neutrality is necessary that the share of energy coming from renewable sources increases. Climate neutrality refers to the idea of achieving net-zero GHG emissions by

balancing those emissions, so they are equal (or less) than the emissions that get removed through the planet's natural absorption.

One option is to increase the exploitation of renewable sources for energy production from 10% in 2019 to values between 35% and 65% within 2050, as reported in the three scenarios proposed by the British Petroleum in Figure 4. [4] At the same time, the share of primary energy produced by fossil fuels has to decrease as fast as possible.

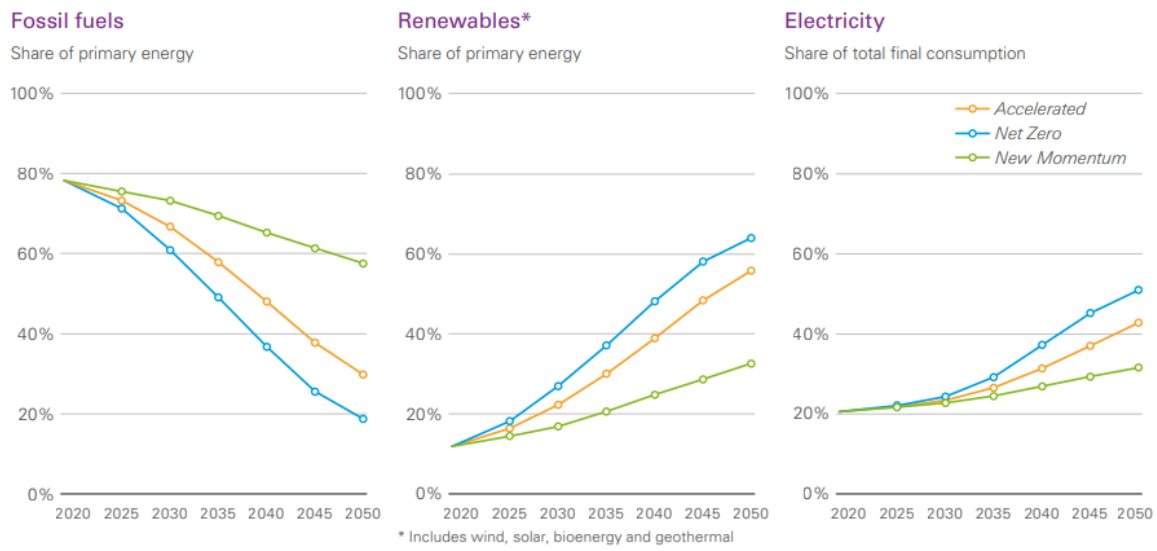

Figure 4 - Future trends for fossil fuels, renewables, and electricity consumption. [4]

In all scenarios, the pace at which the renewable sources penetrate the energetic system is more rapid than any other kind of fuel in history. This is also supported by all the policies that countries are adopting for helping the renewable sources. The increase importance of renewable energy is supported by the continuous electrification of the energetic system. The share of electricity in the final consumption increases indeed, from ca. 20% in 2019 to values between 30% and 50% in 2050, in the three scenarios proposed. [4]

Transition towards a low environmental impact energy system is supported by a rapid growth in low-carbon sources and technologies, such as solar and wind, electric vehicles, biofuels, and hydrogen, as depicted in Figure 5. [6]

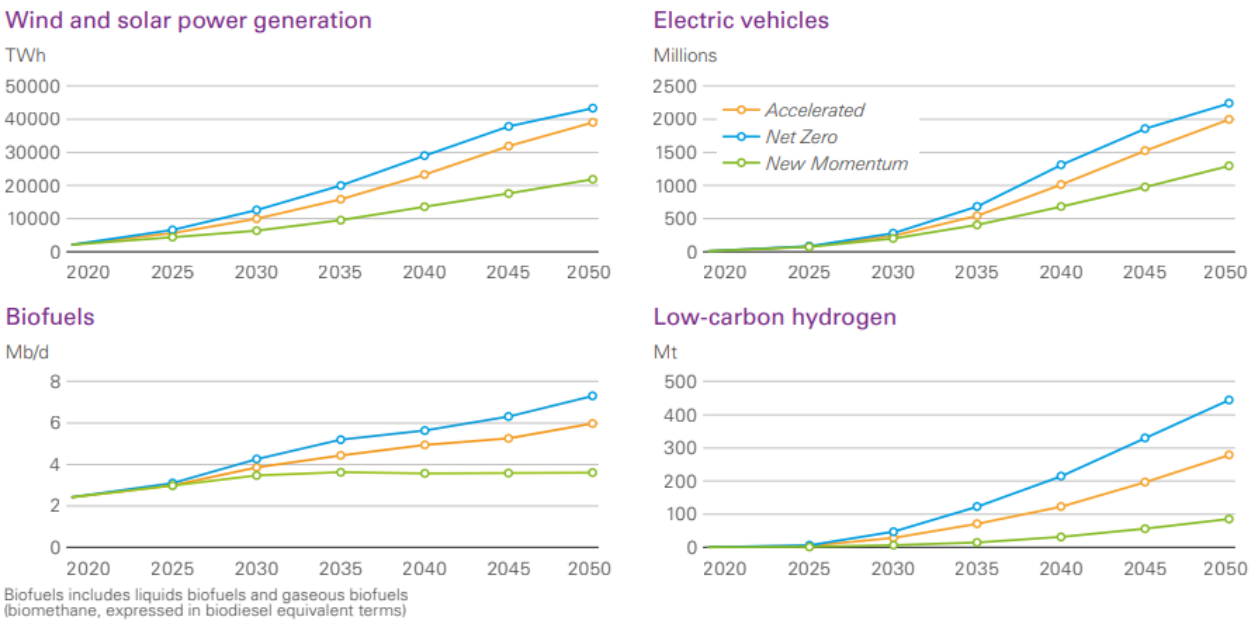

Figure 5 – Future trends of wind and solar power generation, electric vehicles share, biofuels and low-carbon hydrogen proposed by BP Energy Outlook. [4]

A key factor for a sustainable energy transition is represented by the electrification of the transport systems, such as commercial and private. In this light, steps forward are being made at European level, thanks to the new policies regarding the suspension of the production of gasoline vehicles to promote the widespread usage of electric vehicles starting from 2035. [7] Indeed, the transport sector will always require a greater quantity of electric energy as it is pushing towards an abandonment of combustion vehicles to make room for more and more electric vehicles.

As previously said, as well as supported by the predictions of British Petroleum [4], the renewable energy production, especially from eolic and solar sources, is forecasted to grown exponentially and it simultaneously see a decline of the cost, as depicted in Figure 6.

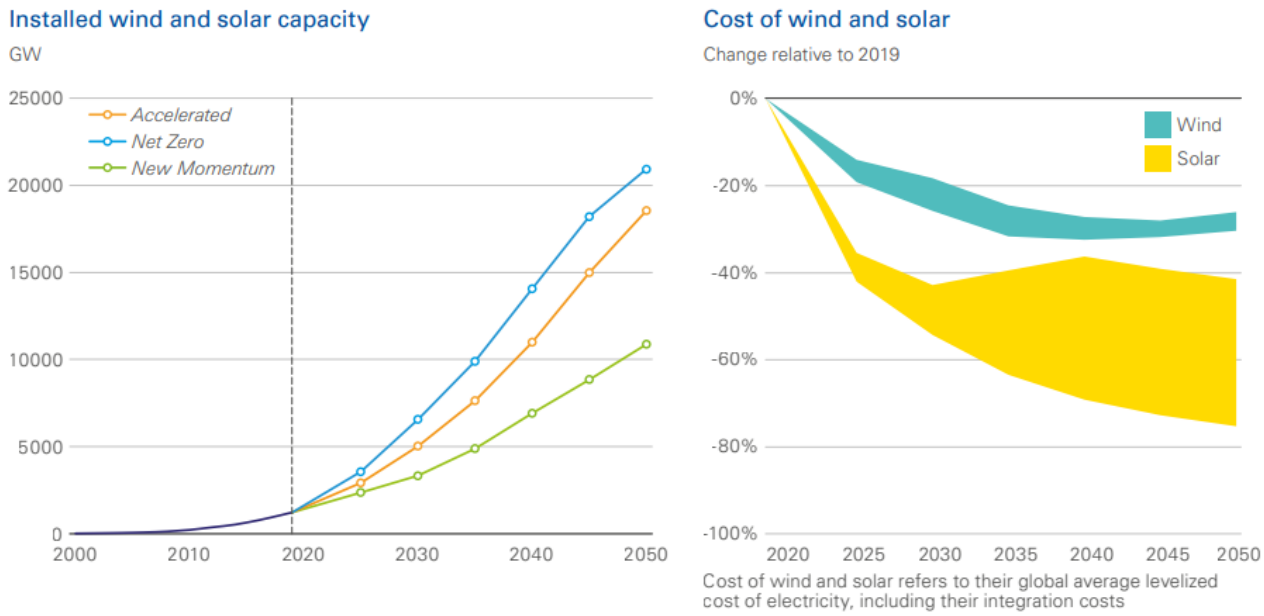

Figure 6 - Future trends of installed capacity and cost of wind and solar proposed by BP Energy Outlook. [4]

A key driver for this trend is represented by the implementation of energy storage systems. Indeed, renewable energy sources, like wind and sun, fluctuate and are intermittent. Hence, in order to ensure electric energy readily available on-demand, to improve the quality and efficiency of energy distribution, and, hence, to decrease the overall cast, the implementation of suitable energy storage systems is mandatory.

Different types of energy storage systems exist nowadays, some of them more suitable for stationary applications while others are suitable for wider applications. In next section there will be descripted most of the energy storage systems to better understand their application field.

1.1 Energy storage systems

Since the world going towards electrification in most sectors, developing efficient and large energy storage systems (ESS), also called accumulators, will become mandatory to manage the daily fluctuations of the energy demand from the grid.

The development of renewable energy sources will be accompanied by an unstable energy supply due to the non-programmability of these sources (for example, the wind, the solar exposure). So, it becomes essential to use storage systems as a solution to the intermittence of these sources, since they will become increasingly important in the next years for a green energy production. As reported in the Energy Storage Market Report from the US Department of Energy, in the coming decade transport and stationary energy storage systems will feature an annual growth 2.5 to 4 TWh/year. As shown in Figure 7, it will mean an increase by three to five times the actual 800 GWh. [8]

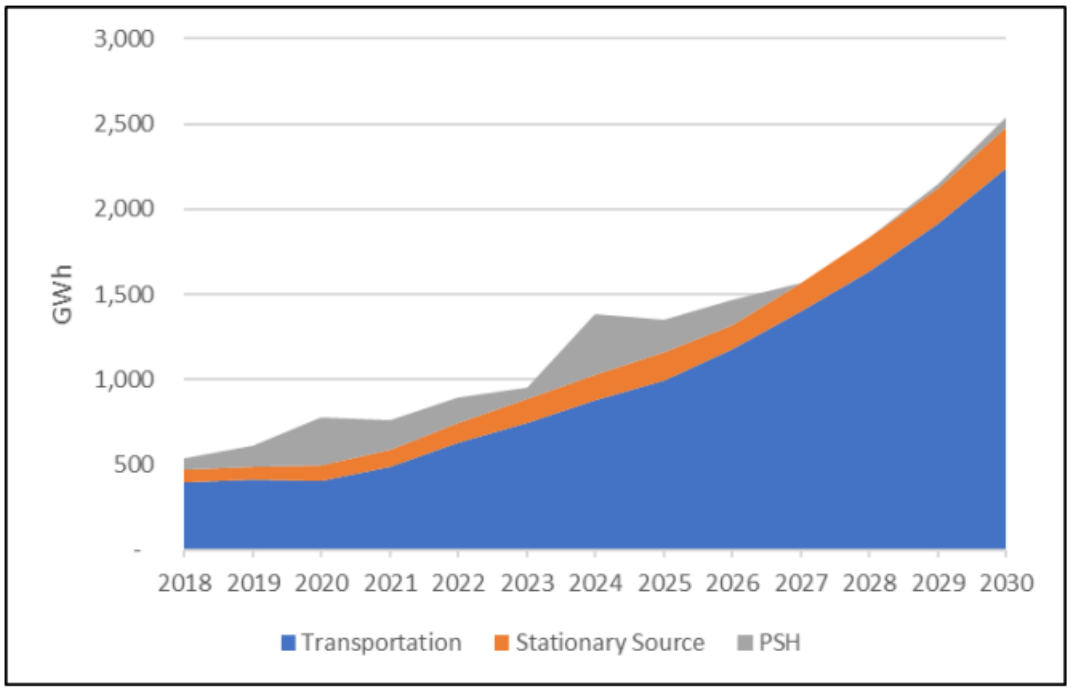

Figure 7 – Future global energy storage trend. [8]

The term “energy storage" means the capture of energy produced at one time in a certain form for use in a different form in a second moment.

Energy storage systems (ESS) can be classified in five main categories:

- Mechanical systems, like Pumped Hydroelectric Storage (PHS) and Compressed Air Energy Storage (CAES).
- Chemical systems, that can store energy by the production of valuable chemicals, like synthetic natural gas (SNG) or hydrogen.
- Electric systems, in which we have capacitors and Magnetic Energy Storage (SMES).
- Electrochemical systems, like batteries (e.g., lithium-ion or flow batteries and supercapacitors).
- Thermal systems, like Phase Change Materials (PCM).

Those systems are usually compared in terms of energy and power density, final usage, storage cost, capacity and maintenance needed. Figure 8 compares different types of ESS. The main difference between them is related to their power and energy density and their time response, which determine their main application field.

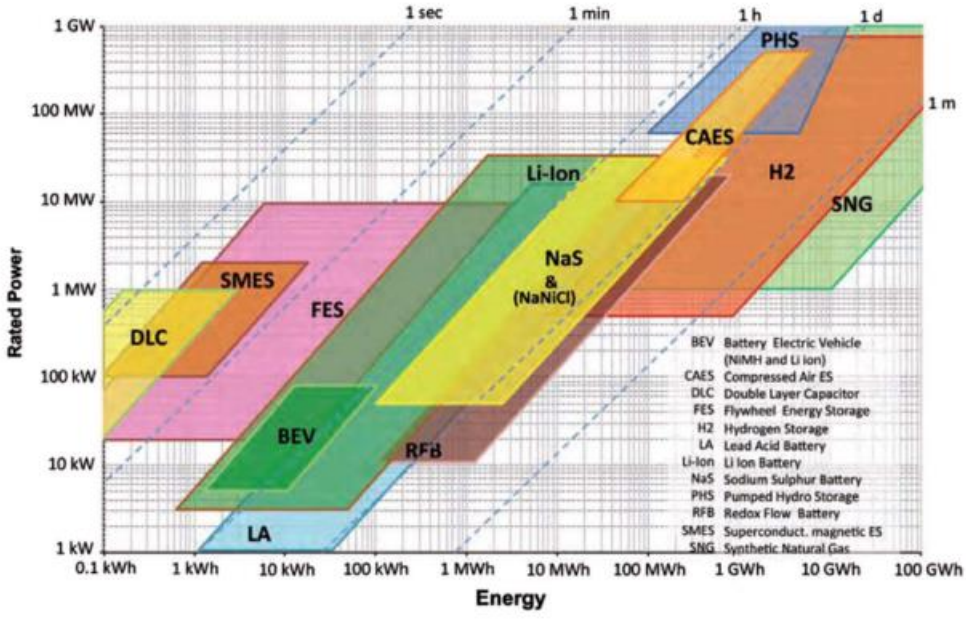

Figure 8 - Classification and assessment of energy storage systems. [9]

Pumped Hydroelectric Storage (PHS)

In PHS, energy is accumulated by moving water between two docks placed at different altitude between a hydroelectric plant, as shown in Figure 9. During the charging phase, when energy needs

to be stored, the plant forces the water towards the dock at high altitude where it is accumulated. Subsequently, when energy is needed, water is flowed down through a hydroelectric turbine to produce energy. PHS is the main type of stationary energy storage currently existing as it features high capacity and low cost per kWh. However, it needs high capital investment for the realization of the plant and an appropriate geographic ground. [9]

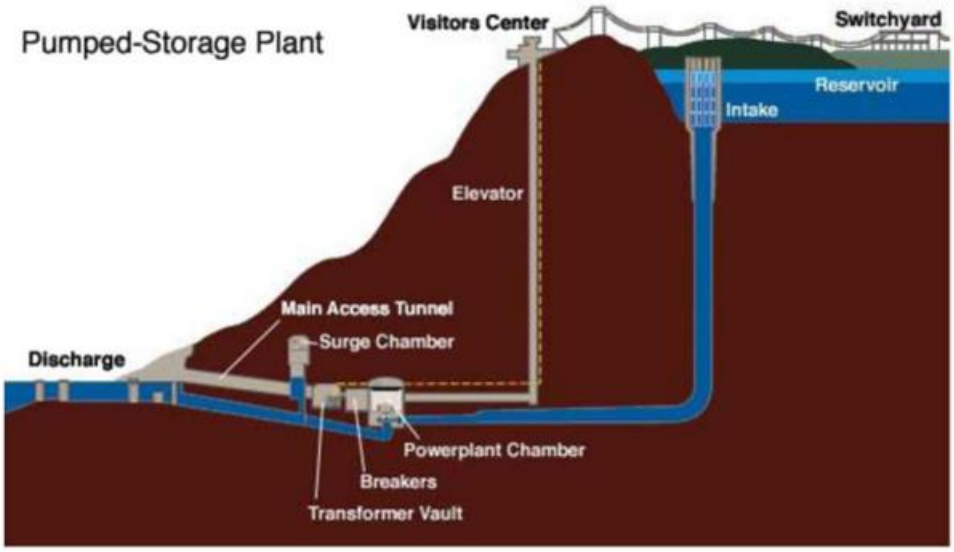

Figure 9 – PHS plant scheme.

Compressed Air Energy Storage (CAES)

In CAES, energetic surplus is used to compress air and store it in underground deposits (like, for example, natural gas/oil exhaust deposits), as depicted in a schematic view in Figure 10. Subsequently, this compressed air is sent to a combustion chamber with a fuel supply, and then the high-enthalpy gas produced during the combustion are expanded in a turbine for electric energy production. Those systems have many advantages such as grid scale potential, flexibility, long life, relatively low operations and maintenance cost, and even a low self-discharge. However, the efficiency of those systems is in the range of 50 to 70%. [9]

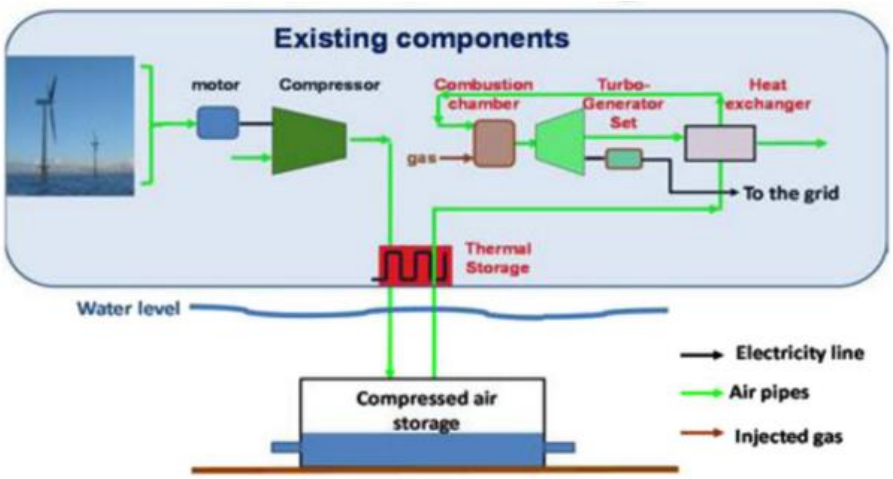

Figure 10 – CAES system schematic. [9]

Superconducting Magnetic Energy Storage

One of the most emerging technologies for energy storage is Superconducting Magnetic Energy Storage, SMES. SMES is based on the concept of superconductivity of certain materials. The so-called superconductors are materials that present almost no electrical resistance, when cooled below a specific temperature called critic temperature. Therefore, an electric current will keep flowing through a superconductor even when the potential between the coil is eliminated.

The main components of a SMES are the magnetized superconducting coil, usually made of niobium titanium alloy inserted in a copper substrate, the power conditioning system (PCS), the cryogenic system, required for cooling the coil below the critic temperature, and the control system. A schematic representation is depicted in Figure 11. The PCS helps regulate, control, and convert the electrical energy during charging and discharging processes, while the control system gets dispatch signals from the grid as well as the coil status and monitors the system's safety.

During the charging phase, current flows in only one direction and the conditioning system must generate a positive voltage through the coil in order to storage energy. In the discharging phase, control system is modified to mimic the system as a load through the coil generating a negative potential which causes the coil to discharge. SMES system are indeed able to respond very quickly. However, it needs expensive plants because the critic temperature to bring materials into the superconducting phase are cryogenics temperatures, approaching 0 K. [10]

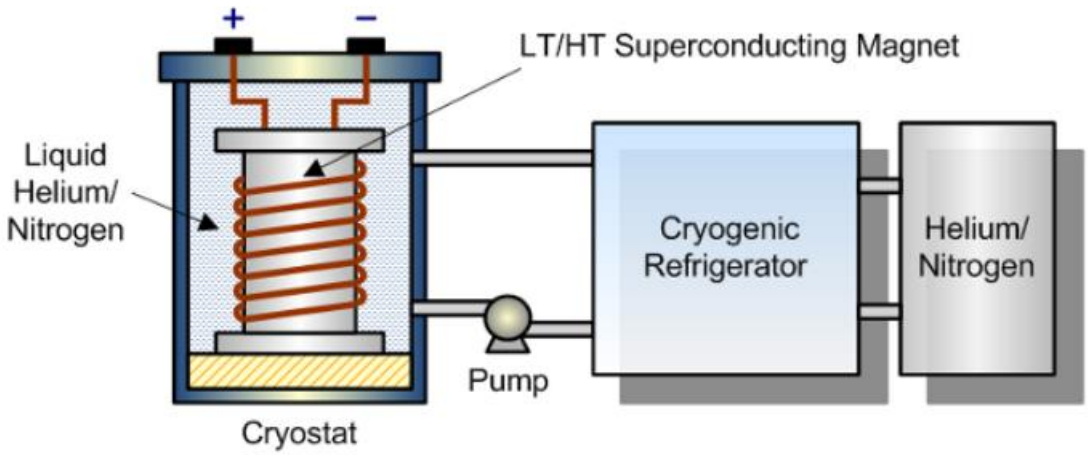

Figure 11 – Superconducting Magnetic Energy Storage schematic representation. [10]

Hydrogen storage and conversion

Hydrogen (H_2) is considered one of the most promising energy vectors of the future. It is not available as H_2 in nature; hence it has to be produced by H^+ reduction. A valuable approach is water electrolysis powered by renewable sources. In addition, H_2 can be exploited to produce electrical energy by the use of fuel cells.

A fuel cell is, indeed, a galvanic cell that converts the chemical energy of a reaction of a continuously supplied fuel and an oxidizing agent into electrical energy. Usually, they are referred to hydrogen-oxygen cells, but other fuels can be employed, like methanol, butane, or natural gas. Inside a fuel cell, like depicted in Figure 12, hydrogen together with oxygen or rather air is converted to steam. For this, two electrodes (anode and cathode) are set in contact with an electrolyte, being separated by an ion-exchange membrane. In proton exchange membrane fuel cells (PEMFC), the fuel is H_2, the oxidant is O_2, and the membrane is a n conductive layer (typically Nafion). PEMFC operates at room temperature and for this reason is extremely interesting for transport applications. During the process, an electrochemical reaction takes place, where H_2 is oxidised to H^+ at the anode, O_2 is reduced to H_2O at the cathode. Inside the cell, protons diffuse from the anode to the cathode. Simultaneously, electrons are released from the anode to the cathode through an external load. The flow of the latter through an external circuit provides electricity. [11]

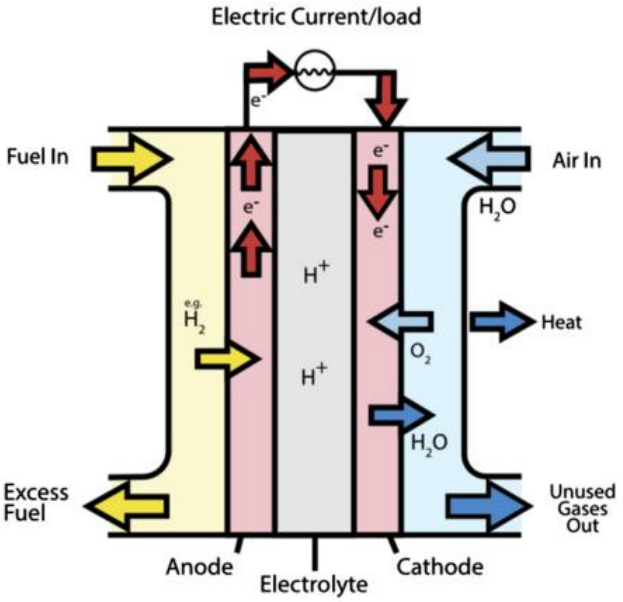

Figure 12 – Basic scheme of a PEMFC fuel cell. [11]

A fuel cell is not a device for energy storage. Instead, it is a converter, but it can be employed to exploit the H_2 chemical energy. Systems designed for storing energy by H_2 production and for its conversion to electric energy by PEMFCs have already been proposed. For example, one of the most adopted technologies is the Regenerative Hydrogen Fuel Cell (RHFC), represented schematically in Figure 13, that stores the energy in the H_2 molecule by electrolysis. In a second time, when electricity is requested, the stored hydrogen is supplied to the fuel cell to generate electricity.

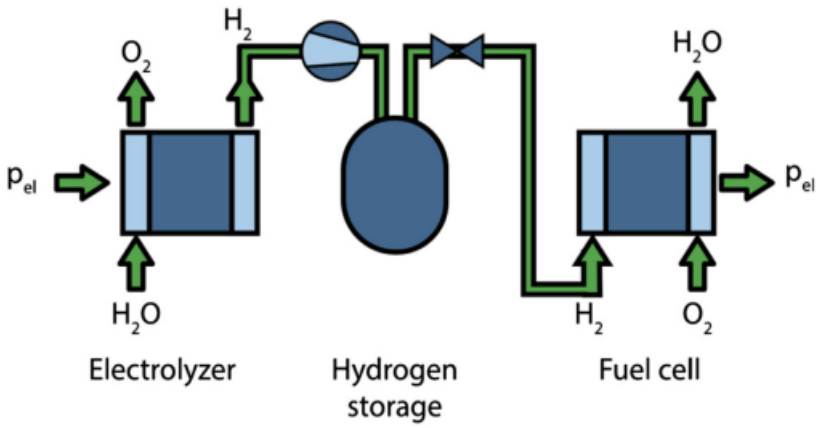

Figure 13 – Schematic of a regenerative hydrogen fuel cell system. [11]

In hybrid energy systems, fuel cells can also be connected to photovoltaics, batteries, capacitors, or wind turbines that supply electricity for electrolysis. To be noted is that electrolysis for the hydrogen production is always energetically disadvantaged unless the electric energy comes from renewable sources and is not needed from the grid. In this case, it is a good way to utilize it for hydrogen production.

Electrochemical energy storage

In the field of storage systems, batteries and supercapacitors are among the most promising technologies as well as the most utilized in different applications. For example, in the transport sector, previously only for the starting of the engine meanwhile today for powering the hybrid and electric vehicles engine, in the industrial sector, for specific industrial equipment, for emergencies and standby power and, lastly in ever-increasing numbers of portable devices, such as phone, computers, toys, radio, …

Figure 14 shows that among the different types of electric storage systems, batteries and supercapacitors are probably the best for stabilizing the grid power fluctuations supplied by renewable sources thanks to their energy and power performance and high conversion efficiency.

The mostly adopted systems are supercapacitors, redox flow batteries and Lithium-ion batteries. They differ in terms of reliability, maintenance, costs (compared to the service power), energy density and shelf life, that are KPI that drive their main application fields.

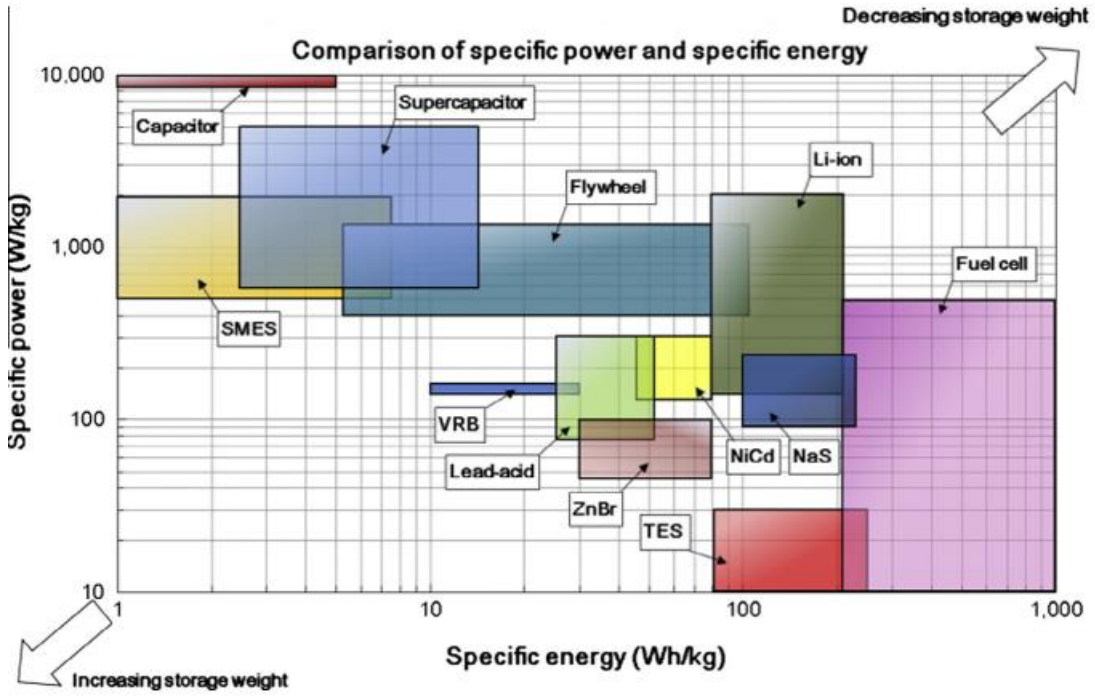

Figure 14 - Comparison of different types of electrochemical storage systems in terms of specific energy and specific power. [12]

Supercapacitors (supercaps) are devices capable of manage higher power compared to batteries. Although supercaps provides hundreds of times the power density in comparison to batteries, they are unable to store the same amount of charge, usually from 3 to 30 times less. This makes supercaps suitable for very specific applications in which a high-power ramp in short times is needed, but high energy density is not required, such as in wind turbines, mobile base stations, electronic devices, and different industrial practices. [13] Another advantage of supercaps is represented by their cycling life. In fact, they can achieve up to several million cycles, as they do not involve irreversible chemical reactions. Like battery systems, supercaps are composed by two electrodes, a separator, and an electrolyte. However, in their conventional form, they store energy by an electrostatic, fast and high-reversible process.

Redox flow batteries (RFBs) are emerging mainly for energy storage in stationary applications. An RFB, as depicted in Figure 15, comprehends three main components: energy storage tanks, the electrochemical cell stack and the flow managing system. RFB utilizes two different electro-active solutions (anolyte and catholyte), separated by an ion-exchange membrane and their functioning is based on the circulation of these two solutions through the cell of the battery. Anolyte and catholyte are composed of two different redox species dissolved in the electrolyte solution. In the discharge mode, anolyte and catholyte solutions flows through the porous carbon collectors and

electrochemically react to generate electrons, which flow through the external circuit. In the cell, the charge-carrying species are transported through a separator (typically an ion-exchange membrane (IEM)), which serves to separate the anolyte and catholyte solutions. [14]

Their possibility of decoupling power and energy in function of their architecture brings to some advantages, such as flexible design and functioning, excellent scalability, moderate maintenance cost and long cycle life. The power density depends on the dimension of the cell, meanwhile the capacity depends on the volume of the tanks filled with the anolyte and the catholyte. On the negative side, redox flow batteries have low power and energy density (< 40 Wh/kg). Furthermore, the most utilized material is vanadium, that has high economic and environment impact, therefore considered by the European Commission as a Critical Raw Material (CRM). [15]

Positive electrode: $VO_2^+ + 2H^+ + e^- \leftrightarrow VO^{2+} + H_2O$

Negative electrode: $V^{2+} \leftrightarrow V^{3+} + e^-$

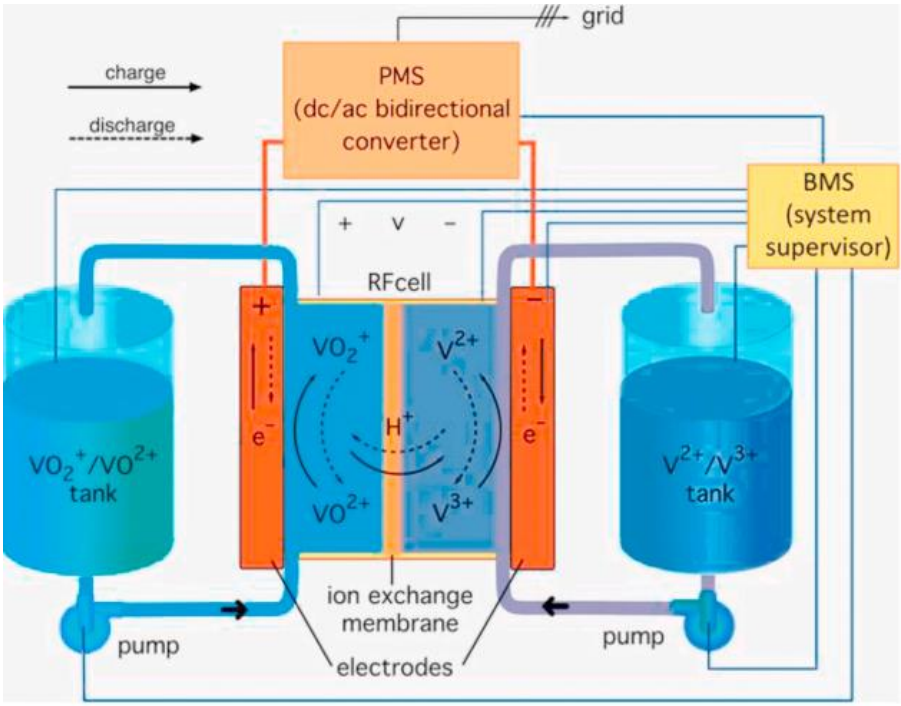

Figure 15 – Schematic representation of a vanadium RFB. [15]

Among batteries, the lithium-ion batteries (LIBs) are those featuring the highest specific energy and for this reason they have revolutionized the sector of electronic technologies and mobility. The future trend of the LIBs predicts a continuous evolution towards the reduction of production cost, the

increase of the energy efficiency and storage capacity. Furthermore, the research is working to make batteries safer and more sustainable, reducing use of toxic and CRM materials while increasing recycling/recovery of the utilized materials.

Moreover, thanks to the reduction of the cost of batteries, electric transport has obtained more consideration and a new mix of renewable electric generation have led to increased interest in the study of LIBs. Indeed, it is expected that the adoption of electric systems on vehicles will grow due to more financial stimulus and costumer incentives provided by states. In particular, the light electric vehicles demand will have a central role towards the development of LIB. Today, about 60% of LIB are indeed utilized for the automotive sector. [16]

However, while the European market is leader in terms of recharge infostructure and electric vehicles, China is nowadays dominating the production market of LIB with almost 80% of the world production capacity. [17]

1.2 Lithium-ion batteries

Lithium-ion batteries (LIBs) are considered among the most performing batteries because they show several advantages such as: [18]

- High cell voltage.
- High specific capacity.
- Good cyclic life.
- No memory effect and long shelf life.
- Excellent coulombic efficiency.
- Possibility to use high discharging currents and complete discharge.

In this section will be explained the functioning and principles of LIBs, the main components, and some way for their recycling.

1.2.1 LIBs functioning

The working principle of lithium-ion batteries is based on the capacity of some materials to reversibly intercalate lithium ions Li^+ inside their crystalline structure. From now on in this thesis, will often talk about the electrochemical cell and is good to specify that a battery is composed by several cells connected in series and/or in parallel. When two or more cells are connected in series their potential is added up, meanwhile the capacity remains the same of a single cell, vice versa when they are connected in parallel their capacity is added up while the potential remains unchanged. This work focuses on the LIB cell.

The cell is composed by two electrodes, connected to an external circuit, separated by an electrolyte, who has the function of ionic conductor. Electrodes are also physically separated by a separator who has the function to prevent physical contact between them, that would result in an internal short circuit.

Figure 16 shows a schematic representation of a LIB. When the cell is completely discharged, the cathode is fully lithiated, in other words the Li^+ ions are hosted inside of his structure. During the charge, Li^+ ions migrate from cathode to anode through the electrolyte. At the same time, electrons flow through the external circuit for reaching anode. The charging process lasts until the cathode has supplied all the Li^+ ions or until the anode is completely lithiated. During the discharge, the process is reversed: ions stored inside the anode flow towards the cathode while electrons, through the external circuit, reach the cathode.

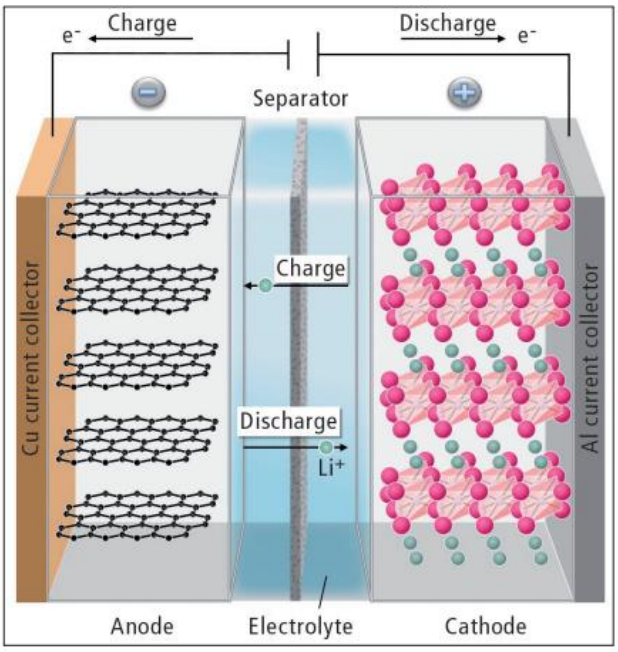

Figure 16 - Schematic representation of LIB. [19]

During discharge, the cathode is the electrode that gets electrons and is reduced, and anode is the electrode that releases electrons and is oxidized. So, conceptually speaking, cathode and anode change their oxidation state and lithiation during the functioning of the battery while keeping (in principle) the same crystalline framework that is required to promote the reversible Li^+ insertion/disinsertion during charge or discharge cycles.

In LIBs, typically the anode is made of graphite. The cathode is a metal transition oxide or phosphate (see Section 1.2.5).

For LIBs made with $LiCoO_2$ as positive electrode and graphite as negative electrode (like the one shown in Figure 16), the chemical reactions for charging and discharging are the following:

$$xLi^+ + xe^- + 6C \leftrightarrows Li_xC_6 \text{ (At the negative electrode)}$$

$$LiCoO_2 \leftrightarrows Li_{1-x}CoO_2 + xLi^+ + xe^- \text{ (At the positive electrode)}$$

where reactions that follow the upper arrow represent the charging process and the ones that follow the lower arrow represent the discharging process. While the overall reaction is as follows:

$$LiCoO_2 + 6C \leftrightarrows Li_{1-x}CoO_2 + Li_xC_6$$

1.2.2 Anodes

As seen in previous section, the anode has the function of store lithium ions in its structure during the charge for then provide them to the cathode during the discharge. Commonly, in LIBs the anode is made of graphite due to its low cost and its ability to intercalate lithium ions. Indeed, graphite can accommodate one lithium ion every six carbon atoms inside its structure with a theoretical specific capacity of 372 mAh/g. [8]

Graphite cycling performance is strictly related to the formation of a stable Solid Electrolyte Interphase (SEI) during the first cycles (in the next section will be explained what the SEI is), which prevents degradation mechanisms likely due to the exfoliation of graphite particles caused by the co-intercalation of solvent molecules during lithiation. [20]

A recent valid alternative to the use of graphite is lithium titanate, $Li_4Ti_5O_{12}$. Despite its lower specific capacity (175 mAh/g) and higher electrode potential (1.5 V Vs Li^+/Li) compared to graphite, it presents good cyclability and a good capacity retention, without volume changes. [21]

Other anodic materials have recently been studied to increase the specific capacity of LIBs, such as silicon and tin, even if they go through large volume variations during the intercalation/deintercalation of lithium ions that lead to stability problems.

For this thesis study the assembled cells were made using metallic lithium as anode.

Metallic lithium features the highest capacity among the whole LIBs anode (3860 mAh/g) and the lowest negative electrochemical potential (-3.04 V vs the standard hydrogen electrode), for those reasons is, in fact, regarded as the “Holy Grail” electrode. [22]

Thus, it is the best electrode for high-energy lithium batteries, but it must overcome the problem of lithium dendrite formation during cycling. Also, lithium has high chemical and electrochemical reactivity in contact with oxygen and water, so it needs controlled atmosphere for its management. Dendrites are formed mostly in lithium metal when the SEI is not homogeneously created in the first cycles (see section 1.2.3). When dendrites grow in the battery there is a reduction on its performance, and an increasing of the safety risk due to the possibility of short circuit.

Innovative solutions are being studied, such as the use of gel or solid-state electrolyte in order to prevent the formation of dendrites. [23]

Beyond what said, metallic lithium has been used in the laboratory for better studying a single electrode property. First of all, lithium is easy to handle and laminate thanks to its malleability. Secondly, it is an electron conductor, so it does not require a current collector or the addition of

carbons nor binders to its preparation. It is sufficient only to laminate it for obtaining a thin layer and then cut it in disk of the required diameter. But, as said before, it is extremely reactive, leading to exothermal reactions in contact with air, indeed lithium must be kept in anhydrous environment, for example a dry box or dry room where levels of water and oxygen are kept below 1 ppm.

1.2.3 Electrolytes

In LIBs, electrolyte plays a key function in the conduction of lithium ions between the two electrodes. In fact, during the operation of the battery, ions move through the electrolyte under the action of the electric field that is generated between the two electrodes.

Electrolyte must be able to perform this function efficiently, without reacting with electrodes or causing other problems that could limit battery life or capacity. Moreover, electrolyte must have a good thermal stability and a low volatility to avoid battery combustion or explosion, and high stability in terms of potential and current battery operating ranges.

Typically, in LIBs, electrolytic solution contains lithium salts dissolved in one or more organic solvents. The most widely employed electrolyte is composed by $LiPF_6$ in ethylene carbonate: dimethyl carbonate (1:1 v/v).

The electrolyte decomposes during the first charge forming a thin film of passivation at the electrode/electrolyte interface: this film, insulant for electrons but conductive for lithium ions, stops further decomposition of the electrolyte while allowing the lithium ions to intercalate into the electrode, without electrons passing into solution. This insulating interface is called Solid Electrolyte Interphase (SEI), sometimes called as Cathode Electrolyte Interphase (CEI) when referred to the positive electrode, and it is generally composed of a mixture of compounds (mainly lithium-based) which depend on the electrolyte composition, temperature, and operating voltage. [24]

An additional positive effect of SEI formed at the graphite anode, is that, if it features sufficiently high Li-ion conductivity, it mitigates the unwanted, side effect of lithium dendrite formation. During charge at high rates and low temperature, metallic lithium might deposit at the graphite surface instead of being inserted. This process might take place where lithium ions encounter a low resistance to electron transfer and not on the entire available surface. Thus, with the succession of cycles, there is a growth of metallic lithium dendrites which, if they manage to reach the counter electrode, cause an internal short circuit which can also lead to a thermal runaway of the cell.

Moreover, a stable SEI prevents further decomposition of the electrolyte which can lead to a series of issues such as: increase of the internal resistance of the cell, excessive heating, diminishing of the ion mobility, gas formation, and over voltages.

1.2.4 Separators

Separator inside the cell has the role of physically separate the two electrodes to prevent a possible short circuit. The material with which the separator is made is chosen according to the materials used for the cell manufacturing, mainly it must be resistant to the solvents used in the electrolyte and stable at the temperatures at which the cell operates. Moreover, it is important that the separator has an adequate degree of porosity so that, once wetted by the electrolyte, it does not hinder the mobility of lithium ions. Eventually, the separator should be as thin as possible to reduce impact to the internal resistance of the cell, usually the thicknesses are between 10-30 μm. A commonly used commercial solution is the so-called tri-layer configuration, where the separator is composed by a sandwich of polypropylene (PP) with a layer of polyethylene (PE) inside.

1.2.5 Cathodes

Nowadays, positive electrode (the cathode during the discharging phase) is made by transition metal oxides with a crystalline structure (stratified or 3D as for spinel) able to accommodate lithium ions and guarantee a rapid diffusion of Li^+ ions during the charge/discharge. However, those materials do not have a good ionic conductivity and the lithium ions, once they get to the interface, can only reach the particle surface that it better exposed to the electrolyte. For this reason, porous or nanostructured materials are used to allow ions to reach the innermost part of the cathode. [24]

Furthermore, also electrons must reach the active sites. So, it must be created a continuous path of conductive material as light as possible by adding carbonaceous particles in small amount (it will be explained better in the next section about the electrode preparation).

Different LIBs are available on the market. Their performance in terms of voltage and capacity is mainly affected by the cathode composition that represents mostly impact on LIBs for several reasons:

- Cost: it is often realized with materials such as cobalt, nickel or manganese. Those materials, and especially Cobalt, a CRM; can be difficult to find, and their cost can vary considerably.

- Thermal instability: often the cathode in those batteries is subject to thermal instability that can bring to safety issues.
- Degradation: cathode is subject to degradation during the use, that brings mainly to an irreversible loss of capacity and an increase of the impedance of the cell. [25]
- Capacity limits: cathode in LIBs has a limited specific capacity far below the anodic one, which means these batteries may be limited in terms of the energy they can store. [26] This is an important factor for electric vehicles application, where the capacity of the battery is fundamental for duration and autonomy.

Table 1 reports the main cathode materials currently employed in LIB manufacturing and their main properties.

Table 1 – Cathode's material commonly employed in LIB. [24]

Cathode material	**Voltage / V vs. Li^+/Li**	**Specific capacity / mAh g^{-1}**	**Volumetric capacity / mAh cm^{-3}**	**Cycle number**	**Energy density / Wh L^{-1}**	**Specific energy / Wh kg^{-1}**
$LiMn_2O_4$	4.0	148	634		270	120
$LiCoO_2$ (LCO)	3.7	137	706	1000	220-350	90-140
$LiNiO_2$ (LNO)	4.0	192	919			
$LiFePO_4$ (LFP)	3.4	170		1000		100

$LiCoO_2$ is the dominant cathode material for LIBs in the portable devices market thanks to its high energy density, excellent cyclic life, and reliability. However, many research groups are looking for different solutions to stop using the cobalt, as toxic and rare material. [27]

$LiMn_2O_4$ is one of the most promising cathode material due to its low cost, non-toxicity and greater security respect to the commercial $LiCoO_2$, even if it presents lower performance and it has the problem of dissolution in the electrolyte solution. [28]

$LiNiO_2$ is a valid alternative to LCO, as it presents a higher energy density, lower cost and there is an abundance of nickel compared to cobalt. However, LNO presents stability problems, both

electrochemical and mechanical, the latter due to volume changes and phase transitions during cell cycling. [29]

Cathodes made with $LiFePO_4$ are relatively safe, have long cycle life and they are stable until 270°C. For those reasons, companies like Tesla are adopting those kinds of cathodes for their batteries. Unfortunately, they cannot operate at high potential. [30]

1.2.6 High voltage cathodes

Energy in a battery depends on the product of its voltage and its capacity, hence, at fixed capacity, the higher the voltage the higher will be its energy density. Therefore, considering that graphite is the mostly used anode material, the higher the potential and the capacity of the cathode the higher the energy of the battery.

As above mentioned, one of the most commonly employed material for cathode in LIB is $LiCoO_2$, which, however, is being tried to abandon due to the presence of cobalt, given its toxicity. Several cobalt-free alternatives have been developed and/or are under development, among which $LiFePO_4$ and $LiMn_2O_4$ are not the best candidates to replace it despite their good thermal stability and their low cost. The main drawback of $LiFePO_4$ is its poor electric conductivity at low temperatures and its low potential of 3.3 V, that limits the energy density. Instead $LiMn_2O_4$ go through large volume changes during the functioning that can lead to mechanical problems.

Four possible solutions are in R&D phase for the realization of high potential cathodes: lithium-rich oxides, nickel-rich layered oxides, LMNO (spinel), and polyanionic compounds (phosphates, silicates, sulphates, etc.), which thanks to their good performance and quite low cost seem to be promising even if there are some obstacles to overcome. In Figure 17a is shown the gravimetric energy densities of conventional and high voltage LIBs paired with graphite and Li-metal anodes that are estimated at material level and cell level, respectively. The gravimetric energy density of high-voltage LIBs could be further improved by replacing the graphite anode with a Li-metal one, in the next section will be explained the use of lithium metal as anode. Meanwhile, in Figure 17b is shown the main advantages and disadvantages of these cathodes. [31]

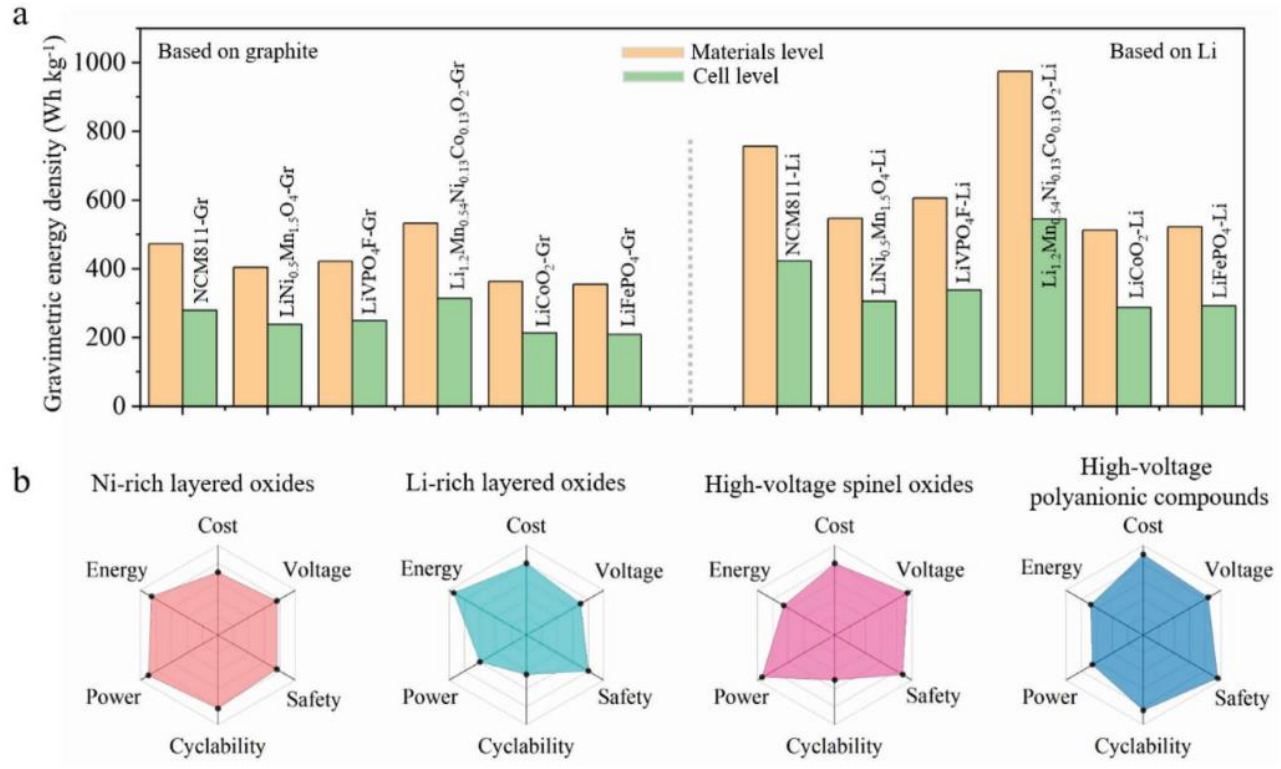

Figure 17 – Performance evaluation of LIBs with various combinations of cathodes and anodes. a) Estimation of the gravimetric energy densities of high-voltage and conventional rechargeable LIBs. b) Radar summary chart of four types of high-voltage cathode materials. [31]

Lithium-rich oxide cathodes possess high reversible capacity (>250 mAh/g) and high energy density (ca. 900 Wh/g). However, phase transition, O_2/Li_2O generation, interface problems and transition metals dissolution are big drawbacks to overcome for their development. As these material problems within a battery result in potential loss, capacity loss and slow charge/discharge.

Nickel-rich layered oxides raised a lot of interest although they tend to suffer from inherent structural degradation and safety issues when charged to a high voltage.

High potential LMNO (spinel) is a great candidate for high potential LIB thanks to its specific capacity of about 130 mAh/g and a working potential of ca. 4.7 V. Compared with the cathodes currently on the market, it can provide higher energy density than all. However, it too presents several obstacles in its development, principally due to the parasitic reactions that occur at the interface between LMNO and electrolyte at high voltages or high temperatures. [32]

Polyanionic compounds deliver a lower reversible capacity than their theoretical capacity. [31]

Figure 18 shows the main obstacles to overcome for the Co-free oxide cathodes commercialization.

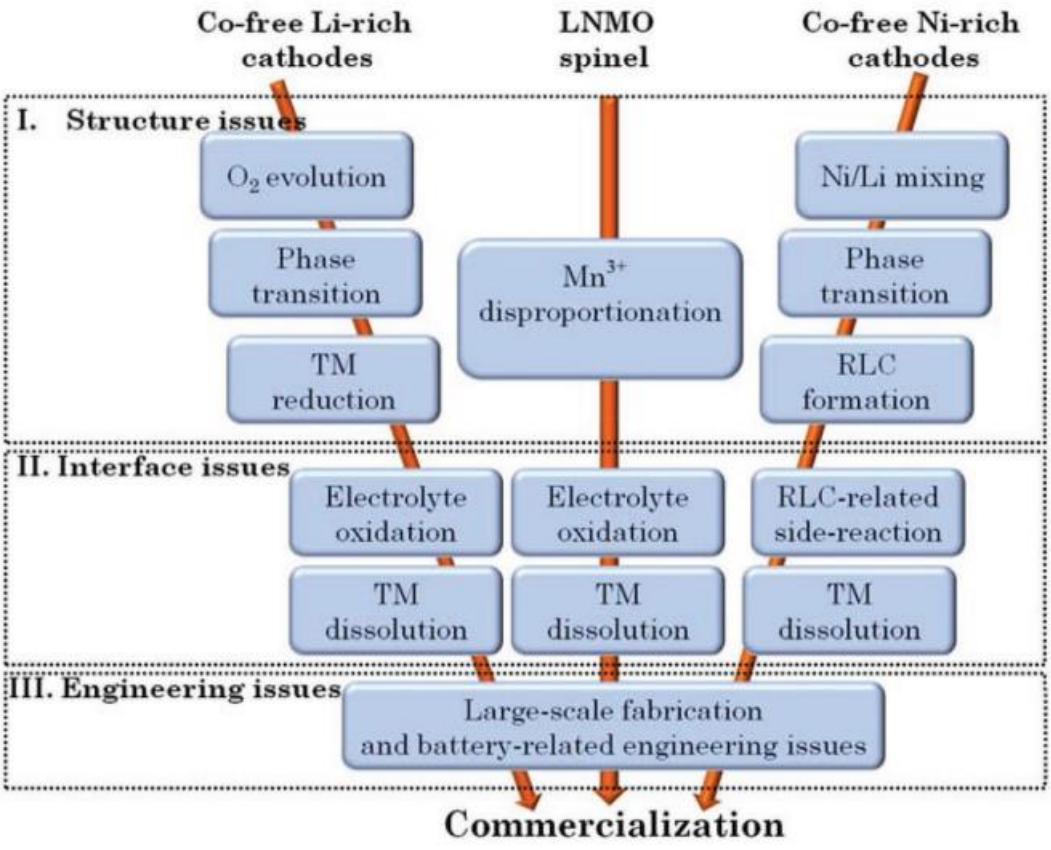

Figure 18 – Obstacles for the industrialization for three Co-free cathodes. [32]

LMNO is the chosen material for the study in this thesis as it will be better described in the subsequent sections.

1.2.7 Electrode processing

Typically, electrodes are prepared by mixing, with different ratio, the active material, the conductive agent, and the binder with a solvent to form a slurry, that is subsequently casted on a current collector (usually aluminium for cathodes and copper for anodes). Despite the percentage of binder is quite low (a formula commonly employed is 90-5-5, active material, conductive agent, and binder, respectively), it is essential for a battery construction. Indeed, the binder has different purposes. It must hold the particles together supporting the adhesion at the current collector. Also, the binder helps to increase the dispersion of particles into the solvent producing a better slurry. Moreover, polymeric binders also offer other functionalities, such as conductivity, stabilization of the CEI and SEI, ecc… [33]

Binders commonly employed are fluorine-based polymers, like poly-(vinylidene difluoride) (PVDF) which has good chemical and electrochemical stability, as well as a good processability. PVDF is one of the most used binders despite is electronically insulating. For this reason, the addition of conductive additives is essential. The main problem caused by the utilization of PVDF in LIBs stands to the solvent NMP (N-methyl-2-pyrrolidone), employed to dissolve PVDF during the slurry preparation. Indeed, it is a toxic organic solvent, harmful both for human health and environment. NMP has been classified as "substance of very high concern" (SVHC) under regulation by EU REACH (Registration, Evaluation, Authorization, and Restriction of Chemicals). [34]

For those reasons, electrodes processed with PVDF need controlled atmosphere and recovery process for NMP, which makes the production of lithium batteries expensive and not eco-friendly. Indeed, many researchers are working on water processable binders for electrodes manufacturing, like cellulose, alginate, pullulan and PEDOT:PSS, in order to create eco-sustainable processes. [35]

In general, like shown in Figure 19, the development of advanced polymeric binders for high energetic density LIBs should take into account the following aspects: water solubility, binder strength, elasticity, conductivity, chemical functionality and wettability by the electrolyte.

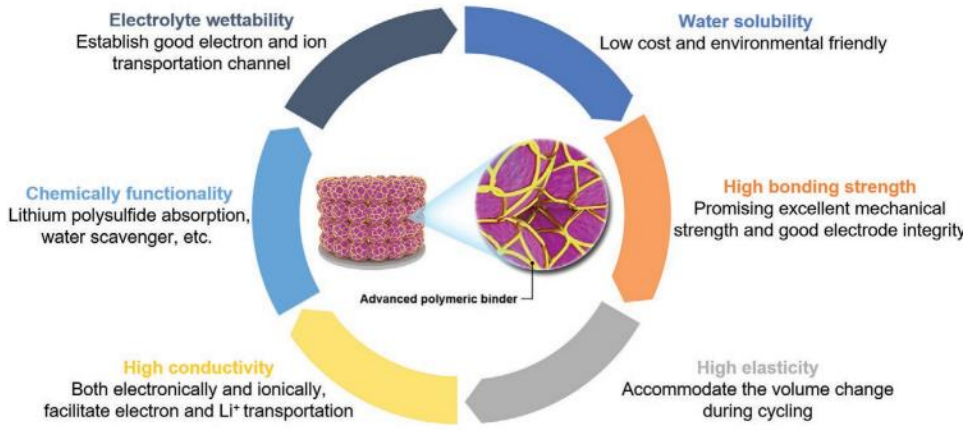

Figure 19 – Ideal properties that an advanced polymeric binder should possess. [36]

1.3 Importance of recycling in LIB

As described in previous sections, there are various critical materials inside a battery, both from a point of view relating to their toxicity, such as NMP and cobalt, and from a socio-environmental point of view, such as rare metals. Cobalt, lithium, and graphite are already in the list of critical raw materials drawn up by the European Commission. [37]

Moreover, rare metal mines, like for example cobalt and nickel, presents various problems:

- Ambiental: extraction requires abatement of trees and removal of ground and rock that can damage natural habitats. Furthermore, production of these metals generates great amounts of toxic waste that can contaminate waters, soil, and atmosphere.
- Working conditions: most mining sites are located in developing countries and are notorious for dangerous and often illegal working conditions.
- Health hazards: metal extraction can cause a poisoning of the air quality that first affects workers in close contact and secondly the surrounding populations.
- China dependency: today China is the main producer of rare metals in the world and the monopoly of the country in the market has created some dependency problems by other countries, including the United States.

Nowadays, LIBs dominate the electric vehicles market thanks to their high energy and power density. LIBs sales have increased of about 16% per year from 1996 to 2016 and the U.S. Energy Information Administration (EIA) predicts that there will be 1.4 million of EV sales in 2035. This high demand of LIBs for EV market will translate in a very high number of exhausted battery packs, estimated to 1 million in 2030 and 1.9 million in 2040. [38]

Those numbers keep tracking of only the vehicles battery, if those relating to portable electronic devices are also considered, it is clear how vitally important the recycling of used batteries will be.

There are three possible options for end-of-life (EOL) EV batteries, according to their design, quality, and state of health (SOH): remanufacturing, repurposing, and recycling. Remanufacturing and repurposing extend the use of LIBs, while recycling ends their life cycle and ensures that valuable materials return to the production chain, partially mitigating the need to extract new raw materials.

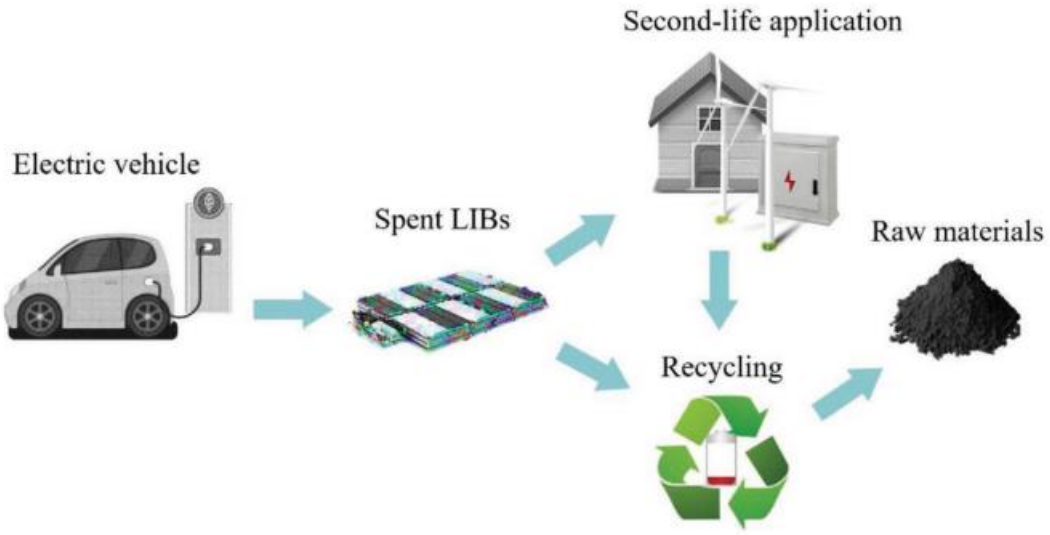

Figure 20 – The second-life application and recycling of LIBs. [31]

Remanufacturing

Remanufacturing process of a LIB consist of the renovation of a battery pack to be able to reuse it in its original application. This requires that the batteries meet requirements relating to their state-of-health, energy, power, cycle life… Remanufacturing involves diagnosis, partial disassembly of the battery packs, replacement of damaged cells or modules within the pack, and finally reassembly into a new battery pack.

Repurpose

Repurpose is another valid option for EOL batteries, where batteries are reconfigured for a "second life" in a less stressful environment, like for example in the stationary energy storage. Repurpose do not comprehend only the substitution of damaged cells or modules, but also the installation of a new battery management system (BMS), for a non-vehicle application. However, the risk and reliability on using batteries not in their original function are not yet well defined. [38]

Recycling

Recycling allows any battery pack to be treated in any state, although it remains a complicated process due to the many chemical species present inside a battery. There are three different technologies for

recycling of a battery: i) pyrometallurgical processes, ii) hydrometallurgical processes, and iii) direct recycling processes.

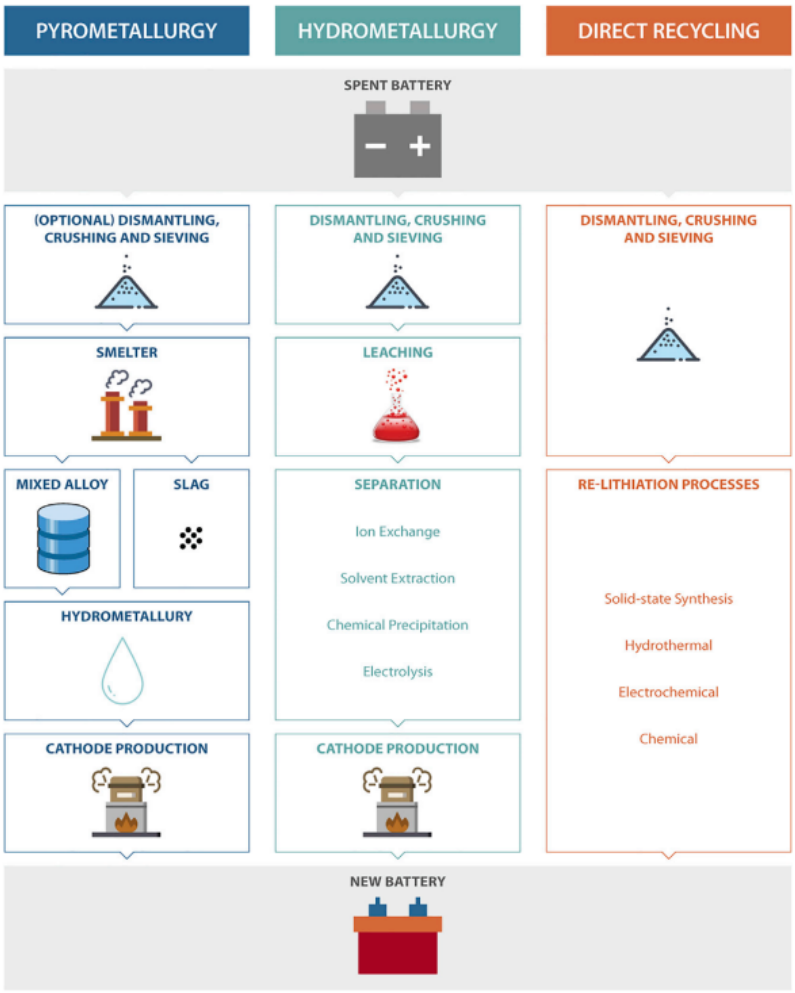

Figure 21 – Three major LIB-recycling processes. [38]

Pyrometallurgy is used to recover precious metals contained inside batteries, such as cobalt, nickel, manganese, and iron. In general, the process involves the treatment of materials inside a furnace at high temperature, which allows the separation of metals from other substances present in the battery.

The process involves several steps. In the first place, batteries are broken down into a mixture of materials through a smelting process. During the smelting, the material mixture is heated to high temperatures, which allows the metals to melt and separate from the non-metallic materials which are incinerated, such as plastic components and all organic compounds. Subsequently, the separated metals are refined through chemical-physical transformations, in which the metals are further separated and purified. The refining process is necessary to remove any impurities and contaminants that may be present in the recovered metals.

Lastly, recovered metals are melted and solidified into ingots or other usable forms, so that they can be used to make new batteries or other products. [39]

Hydrometallurgy processes consists of various steps: [40]

1. Decomposition: the battery is disassembled, and the components are broken down so that valuable materials are isolated.
2. Comminution: the battery components are ground to obtain small fragments, in order to increase the contact surface between the materials and the solution.
3. Leaching: battery fragments are placed in contact with an acid or basic solution, depending on the type of battery and on the materials that are to be recovered. The solution reacts with materials and extract valuable components, which they pass into solution.
4. Material recovery: valuable materials are separated from the solution by processes such as solvent extraction, chemical precipitation, and electrochemical deposition. However, the leaching solution composition is very complicated, and it results difficult to separate all valuable metals with just a single method. Indeed, it is necessary to use two or more methods for metals separation.
5. Refining: recovered materials are subject to refining processes to obtain high purity products.

Hydrometallurgy process is the most utilized for treating exhaust LIBs as it is considered as the most suitable for their recycling.

Direct recycling is a proposed recovery method for direct collection and recovery of the active materials contained inside batteries, preserving their original crystalline structure. In this process, battery components are firstly separated, principally using physical separation methods, magnetic separation, and a moderate thermal processing, to avoid the chemical degradation of the active materials. Subsequentially, active materials are purified, and both the superficial and bulk defects are repaired by re-lithiation or hydrothermal processes. However, direct recycling process is still in laboratory phase and more work are needed for its commercialization. [38]

1.4 Thesis aim

This thesis work has been carried out at the Laboratory of Electrochemistry of Materials for Energetic (LEME) of the Department of Chemistry "Giacomo Ciamician" of the University of Bologna (UNIBO) in collaboration with MIDAC S.p.A., an Italian company that became one of the European leading companies in the field of batteries with more than 25 years of experience. It is a collaborative project set between MIDAC S.p.A., partner of the IPCEI/012/00B2 EuBatIn program and GISEL – INSTM, Consorzio Interuniversitario Nazionale per la Scienza e Tecnologia dei Materiali (Research unit: UNIBO), as well as within the PNRR Project CNMS-Spoke 13-MOST (Code: CN00000023) that targets the development of new materials and sustainable processes for the production and recovery of current and next generation high performance electrochemical cells for energy storage/conversion.

The purpose of this thesis is, indeed, the study of the formulation of Cobalt-free, high voltage cathodes for lithium-ion batteries. It addresses the MIDAC need of setting an electrode manufacturing and testing process that will be used to assess the performance of the cathodes that they will produce by exploiting recycled materials from spent batteries.

Specifically, I have carried out a comparative study of the electrochemistry properties of $LiNi_{0.5}Mn_{1.5}O_4$ (LMNO)-composite cathodes produced with different formulations. The electrodes featured a commercial LMNO powder and were formulated by blending this active material with carbon conductive additive and different binders, and by modifying the mass ratios of the components. The electrode performance was evaluated using the benchmark electrolyte LP30 that is used, today, in commercial lithium-ion batteries. It is a solution of lithium hexafluorophosphate dissolved in mixture of ethylene carbonate – dimethyl carbonate.

2. Materials and methods

In this chapter, the materials utilized, and the electrochemical test performed for the characterisation of the cathode are reported.

2.1 Materials

2.1.1 LMNO powder

The $LiNi_{0.5}Mn_{1.5}O_4$ (LMNO) powder employed for preparing the lithium-ion battery cathodes is the commercial one from NANOMYTE® SP-10 (NEI Corp.). Table 2 reports the specifics of the LMNO powder from the datasheet of the material provided by the Company.

Table 2 - Characteristics and recommended operating conditions of the LMNO powder from NEI Corp.

Material characteristics

Product Description	Lithium Manganese Nickle Oxide (LMNO) powder
Formula	$LiMn_{1.5}Ni_{0.5}O_4$
Average particle size (D_{50})	4 – 7 µm
Specific surface area	1 - 2 m^2/g

Electrical characteristics

Nominal voltage vs. Li/Li^+	4.7 V
Minimum capacity	115 mAh/g
Experimental capacity	≥ 125 mAh/g (3.5 – 5V @ 0.1C)

Recommended operating conditions

Maximum charge voltage	5.0 V vs. Li/Li^+
Maximum charge current	3C
Cutoff voltage for discharge	3.5 V vs. Li/Li^+
Maximum discharge current	3C

2.1.2 Binders

As commented in section 1.2.7, electrode binders are essential for the battery and they affect the battery performance. In this thesis two types of Polyvinylidene fluoride (PVDF) binders were employed for the electrode preparation. Table 3 reports the binders employed in this thesis work, as well as their chemical formula, producer and physical state.

Table 3 – Composition of binders.

Name	Chemical formula	Producer	Physical state
PVDF Kynar	$(CH_2CF_2)_n$	Arkema	Powder
PVDF Solef 5130		Solvay	Powder

2.1.3 Separator

Two different separators were used in the electrochemical cells, and they are described in Table 4. Celgard 2300 is a trilayer based on polyprolyene (PP) and poliethilene (PE). It is already employed in the battery manufacturing market. Whatman GF/A is a glass microfiber mat. It is not used in commercial cells but being extremely inert and easy to be impregnated with the electrolyte, is very useful for preliminary tests. The Whatman GF/F separator was employed only in EL-Cell cells (difference of the assembled cells will be explained in the next Chapter).

Table 4 – Description of the separators.

Name	Material	Thickness	Producer
Whatman GF/A	Glass microfiber	0.26 mm	Whatman
Whatman GF/F	Glass microfiber	0.42 mm	Whatman
Celgard 2300	Trilayer (PP and PE)	30 µm	Celgard

2.1.4 Other materials

Table 5 reports other materials that have been used in this study. N-Methyl-2-pyrollidone (NMP) was used to solubilize PVDF and prepare the cathode slurries. The carbon C65 was used as conductive additive to promote electron transfer between the LMNO particles and between the active layer and the current collector (an aluminum foil). Water MilliQ was used to treat the aluminum foil before use (see Section 2.2.1). The electrolyte adopted for the tests was 1M $LiPF_6$ in ethylene carbonate: dimethyl carbonate 1:1 (v/v) (LP30).

Table 5 – Other materials employed.

Name	**Function**	**Producer**	**Chemical formula/composition**
N-Methyl-2-pyrollidone (NMP)	Solvent	Merk	C_5H_9NO
C65	Conductive carbon	Imerys	C_{65}
LP30	Electrolyte	(Selectilyte BASF, German	1M $LiPF_6$ in ethylene carbonate: dimethyl carbonate 1:1 (v/v)
Milli-Q water	Washing agent	Produced by MilliQ equipment	H_2O

2.2 Methods

2.2.1 Electrode preparation

Electrodes were produced by casting LMNO-slurries on aluminium current collectors (20 μm-thick). Before casting, aluminium foils were treated to remove passivation layers. Specifically, the foils were washed for 5' in a KOH 5% solution, washed with MilliQ water, and dried in a thermostatic oven at 80°C.

The preparation steps were always the same, but with different parameters which they will be defined in Chapter 3. In general, for the slurry preparation, a solution of PVDF and NMP was initially stirred. Then, the LMNO and C65 powders were added to the binder solution and milled in a planetary miller (FRITSCH, Pulverisette) using a tungsten jar (12 mL) and spheres (5 spheres, 5 mm diameter).

The slurry obtained was, then, coated on the aluminium foil by a Mini Coating Machine (Hohsen Corporation) at 0.3 $cm\ s^{-1}$ and with a bar distance of 8 mil. An example of the composite cathode layer cast on aluminium foil is given in Figure 22.

Subsequentially, the coated films were dried at 60°C overnight in a thermostatic oven. Electrodes were cut from these films, pressed at different pressures, and dried again under dynamic vacuum (BUCHI oven) for 12 hours at 120°C to eliminate any NMP trace. Finally, all electrodes prepared were transferred in a dry box under argon atmosphere (MBraun, H_2O e O_2 < 1 ppm).

Figure 22 – LMNO composite cathode slurry casted on the aluminium foil.

2.2.2 Electrochemical test

LMNO electrodes (9 mm diameter) were tested in 3-electrode Swagelok cells in Teflon with AISI 316 connectors or in 2-electrode EL-Cell cells (GmbH, Germany). Figure 23 shows the two types of cells used to perform the electrochemical tests. The 3-electrode Swagelock cells were used to perform the main tests that were carried out in half-cell configuration, i.e., by using a lithium metal reference electrode and a lithium disk as counter electrode. The EL-Cell was assembled for measuring the pressure evolution inside the cell, related to CEI formation, and only 3 cyclic voltammetries at 50 μV/s were performed on this kind of cell. For these tests, the same lithium disk was used as reference and counter electrode.

For both cells, lithium metal was mechanically cleaned to remove any passivation layer before using. Before the assembly of cells, separators were soaked with 1M $LiPF_6$ in 1:1 (v/v) ethylene carbonate (EC): dimethyl carbonate (DMC) (LP30, Selectilyte BASF, Germany) electrolyte. Celgard separators were soaked overnight before assembling while Whatman for just 2-3 hours, because, since Whatman is made of glass fiber, too many hours immersed in electrolyte can lead to flaking of the separator. The cells were assembled inside a dry box with Argon atmosphere (MBraum, H_2O and O_2 < 1ppm).

The electrochemical measurements were carried out by a multi-channel VMP (Perkin Elmer, Waltham, MA, USA) potentiostat/galvanostat.

The Li/LMNO Swagelok cells were tested by the following protocol:

- 2 galvanostatic charge/discharge cycles at C/10 carried out to form a stable CEI (Cathode Electrolyte Interphase).
- 2 (or 3) cyclic voltammetries at 50 μV/s to detect any side electrochemical signals that could impact on cycling performance of the cell.
- A series of galvanostatic cycles run with the same charge current (C/5) and different discharge currents (C/5, C/3 and C/1) to evaluate the capacity retention at different currents.
- Repeated charge/discharge cycles at C/1 to evaluate the cell cycle-life.

The Li/LMNO EL-Cell was assembled for measuring the pressure inside the cell and only 3 cyclic voltammetries at 50 μV/s were performed on this kind of cell.

The galvanostatic tests were performed with charge and discharge cut-off voltages of 5 V and 3.5 V, respectively. The C-rate current was set referring to the experimental specific capacity claimed by the LMNO manufacturer, i.e. 125 mAh/g.

After calculating the LMNO mass [g] available in 0.63 cm^2 of the cathodic area, the electrode nominal capacity was obtained by eq. (1).

$$Electrode\ nominal\ capacity = \frac{m_{LMNO} * 125}{1000}\ [mAh] \quad (1)$$

Hence for a 1C rate, the current in mA results by eq. (2):

$$1C\ current = \frac{Electrode\ nominal\ capacity}{1h}\ [mA] \quad (2)$$

a)  b) 

Figure 23 – Electrochemical cells used for electrochemical tests: a) Swagelok cell and b) EL-Cell

The PAT-Cell-Press is a pressure test cell for measuring gas evolution and drawing gas samples (optional). Its advanced design includes a laser welded pressure sensor and glass-to-metal seals. The PAT-Press-Box is required to read and record the analog pressure signal of a PAT series test cell when the cell is used in a docking station that does not provide this functionality itself. The box is placed between the docking station and the used potentiostat, as depicted in Figure 24.

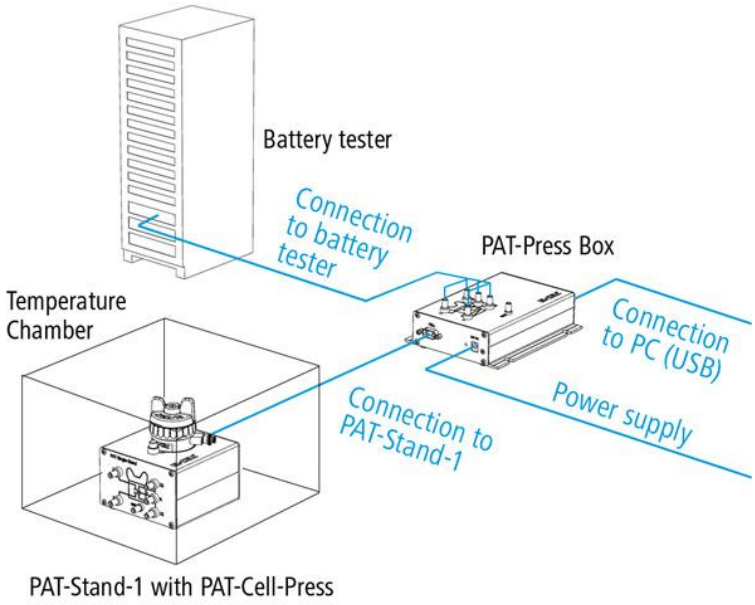

Figure 24 – Schematic representation of the EL-Cell and PAT-box setup.

3. Results

This Chapter presents the results of the test conducted on the LMNO electrodes prepared by different compositions. As first, it will be reported the results of the benchmark electrode, realized with Kynar PVDF produced by Arkema. Then, the results obtained by LMNO electrodes realized with Solef PVDF produced by Solvay. Different mass ratios were tested with Solef PVDF, as it will be explained in next sections. The gas evolution during CEI formation has been also exploited for Kynar PVDF-based electrodes.

3.1 Electrode compositions

The procedure adopted for the electrode manufacturing was similar for all samples, as described in Section 2.2.1 All the electrodes were produced by casting slurries based on LMNO and carbon (C65) disperded in a solution of PVDF (binder) in NMP (Solvent). The electrode preparation steps are detailed for each batch in the following sub-sections.

Table 6 summarizes the code and the composition of the different LMNO cathodes. It also reports the NMP volume to LMNO mass ratio set to formulate the slurries that were coated on aluminum foil current collectors. Specifically, at first the Kynar PVDF-LMNO electrodes (K-LMNO) were tested as a benchmark. K-LMNO cathodes featured 80% LMNO, 10% PVDF and 10 % carbon conductive additive (C65). Then, a different polymeric binder Solef PVDF was investigated in different mass ratios (S-LMNO) of LMNO, binder, and C65 carbon.

Table 6 – Code, composition in. terms of LMNO, binder and carbon mass percentage, and, and solvent (NMP) - to LMNO mass ratio manufacturing processes description of the LMNO cathodes.

Code	LMNO [%]	Binder [%]	Carbon [%]	Solvent (NMP) – to LMNO mass ratio	Notes
K-LMNO	80%	Kynar PVDF 10%	C65 10%	4.2	Ball milling at 250 rpm
S-LMNO1	80%	Solef PVDF 10%	C65 10%	4.1	Ball milling at 300 rpm
S-LMNO2	90%	Solef PVDF 5%	C65 5%	3.7	Ball milling at 300 rpm
S-LMNO3	85%	Solef PVDF 7.5%	C65 7.5%	3.9	Ball milling at 300 rpm

3.1.1 K-LMNO

3.1.1.1 K-LMNO electrode preparation

Initially, Kynar PVDF was dissolved in NMP by stirring overnight. Then, the binder solution was added in a jar with LMNO and C65 powders for the ball milling process at 250 rpm for 90 + 90 (reverse) minutes. The obtained slurry was casted on the aluminium current collector. The coated film was dried at RT for the weekend, then for few hours at 80°C in a thermostatic oven before cutting and pressing at 4 Ton/cm^2, and dried again under dynamic vacuum (BUCHI oven) for 12 hours at 120°C to eliminate any trace of NMP. The final composition of the K-LMNO cathodes was: 80% LMNO, 10% C65, 10% Kynar PVDF.

With this formulation 6 electrodes were prepared with the total (including aluminum), composite and LMNO loadings reported in Table 7. Electrodes A11, A13 and A15 were tested in Bola cell and the A16 in the EL-Cell cell. In following Section 3.1.1.2 will be reported the data about the A11 electrode and in Section 3.1.1.3 the data about the A16 electrode.

Table 7 – Code, total (including aluminium foil), post vacuum heating, composite and LMNO masses of the K-LMNO electrodes.

Electrode's code	Aluminum and composite mass post vacuum heating [mg]	Composite mass [mg]	LMNO mass [mg]
A11	5.20	2.32	1.86
A12	5.69	2.81	2.26
A13	5.40	2.52	2.02
A14	6.09	3.21	2.58
A15	6.07	3.19	2.56
A16	3.97	1.85	1.48

3.1.1.2 K-LMNO electrode electrochemical tests

In order to carry out the electrochemical tests, a Bola cell with K-LMNO was assembled. The Li/LP30/K-LMNO cell, featuring Whatman GF/A as separator, was tested following the protocol described in section 2.2.2. The C-rates used for the cell was calculated following what it has been said in section 2.2.2 and, hence, by equations (3) and (4).

The LMNO mass on the electrode:

$$m_{LMNO} = composite\ mass * LMNO\% = 2.32 * 0.8 = 1.86\ mg \quad (3)$$

Therefore:

$$Electrode\ nominal\ capacity = \frac{125 * 1.86}{1000} = 0.233\ mAh \quad (4)$$

where 125 mAh/g is the theoretical capacity of LMNO claimed by the manufacturer.

Thus, we have C/1 current = 0.233 mA, C/3 current = 0.078 mA, C/5 current = 0.047 mA and C/10 current = 0.0233 mA.

Figure 25 and Figure 26 report the electrode potential profiles recorded during the conditioning galvanostatic charge-discharge cycles performed at C/10, for the electrode A11. Figure 27 depicts

the differential capacity profile dQ/dE vs the electrode potential V, where the peaks (or inflection points) mean that a phase transition due to the lithiation/de-lithiation is occurred. [41]

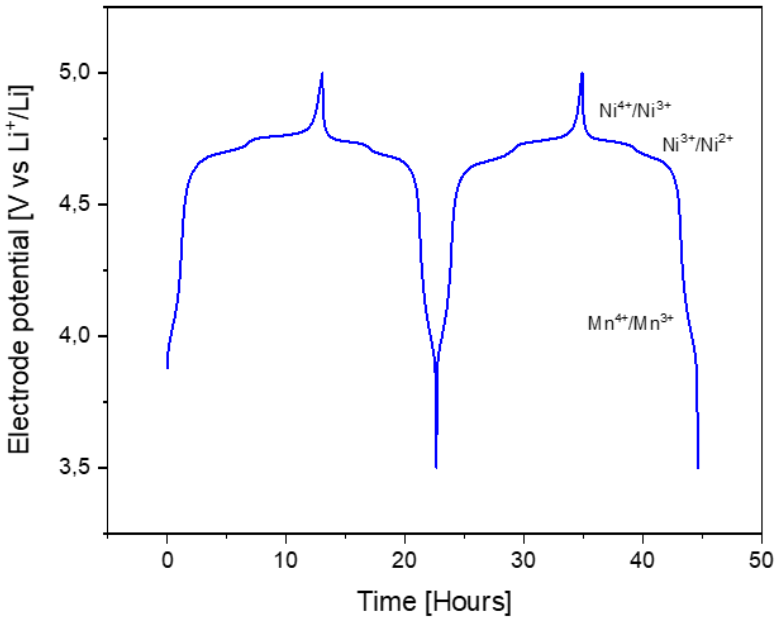

Figure 25 – Electrode potential profiles as function of time of the two conditioning cycles at C/10 of the K-LMNO cathode A11.

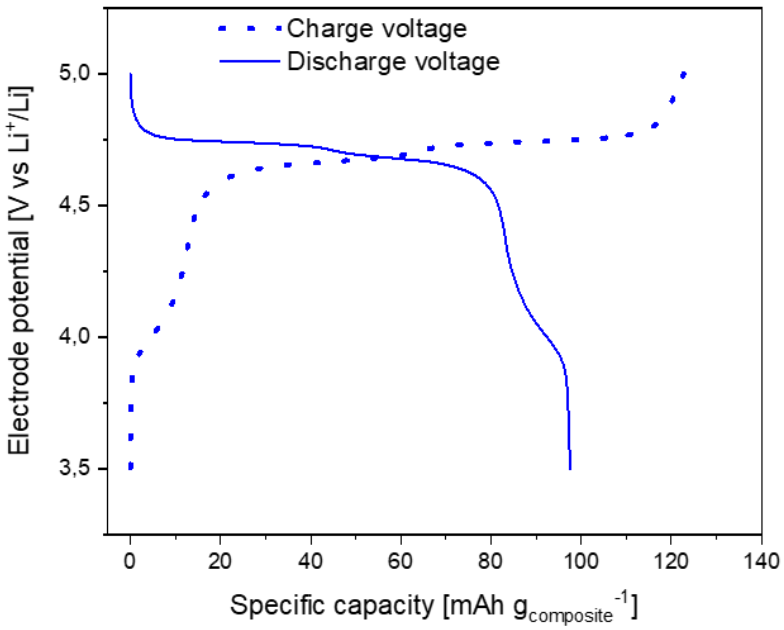

Figure 26 – Charge and discharge electrode profiles of the second cycle as a function of the cycled composite capacity of the K-LMNO cathode A11.

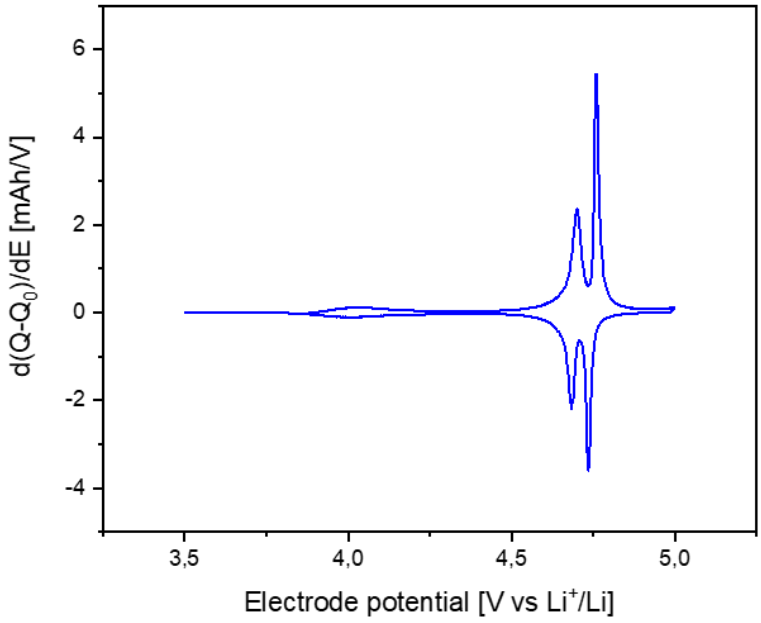

Figure 27 – Differential profile of d(Q-Q0)/dE of the second galvanostatic charge-discharge cycle at C/10 reported in Figure 25.

Table 8 reports the values of the charge and discharge capacities in mAh evaluated by this test. It also reports the values of the discharge capacity normalized to the composite and LMNO mass loading, and the coulombic efficiency. Coulombic efficiencies of the first cycles are not near the usual values (around 95-99%) because during the first operating cycles happen the formation of the CEI.

Table 8 – Charge and discharge current (I), charge (Q_c) and discharge (Q_d) capacities in mAh, discharge capacity normalized to the composite ($Q_{composite}$) or LMNO (Q_{LMNO}) mass loading, and coulombic efficiency (η) evaluated from the conditioning cycles for the electrode A11.

Cycle	I [mA]	Q_c [mAh]	Q_d [mAh]	$Q_{composite}$ [mAh/g]	Q_{LMNO} [mAh/g]	η [%]
1	± 0.0233	0.303	0.223	96.12	119.89	73.6
2	± 0.0233	0.285	0.226	97.41	121.51	79.3

Figure 28 reports the cyclic voltammogram (CV) with current normalized to the composite mass of the electrode. The CV's shape is like expected for LMNO, with reversible peaks at ca. 4V, 4.7 V and 4.8 V. These peaks can be assigned to the Mn^{3+}/Mn^{4+}, Ni^{2+}/Ni^{3+}, and Ni^{3+}/Ni^{4+} redox couples,

respectively. [35] These peaks also define the voltages plateau in the galvanostatic profile of LMNO cathodes highlighted in Figure 25 and Figure 26.

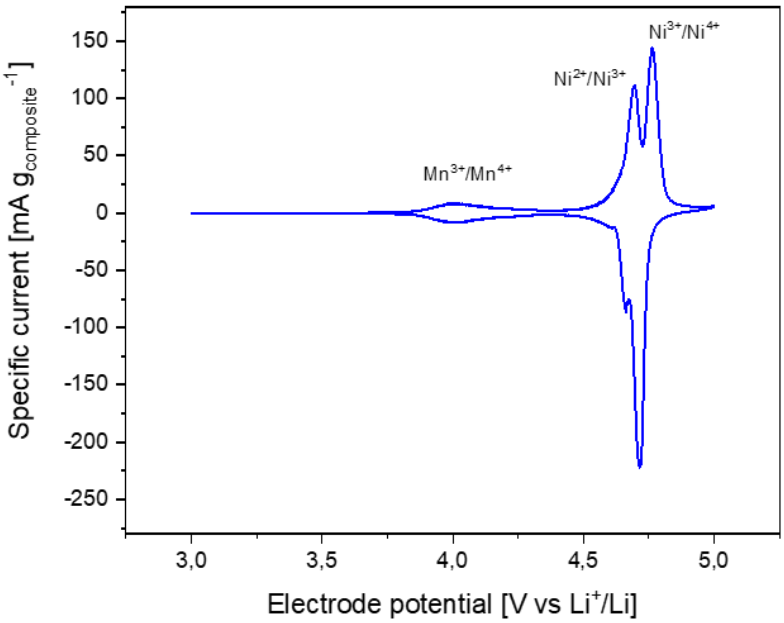

Figure 28 – Cyclic voltammetry of K-LMNO cathode A11 at 50 µV/s normalized to the composite current.

After conditioning and CV, the rate response has been evaluated. Figure 29 reports the voltage profiles at different discharge C-rates (C/5, C/3 and C/1) while the charging current were always the same (C/5). Figure 30 reports the specific capacity normalized to the LMNO mass and the coulombic efficiency at each C-rates. In Table 9 are reported the capacity and coulombic efficiency delivered at each C-rate. It is important to note the constancy of the capacity at each C-rates, basically it does not decrease while increasing the discharge current, but it remains constant around values of 0.235 mAh. Also, the LMNO specific capacity evaluated by this test appears to be little higher than the theoretical one used for calculating the C-rates. The capacity exhibited at the first cycles at C/10 is lower than the following presumably because CEI was still forming. CEI formation was further investigated by A16 cathode as described in the Section 3.1.1.3.

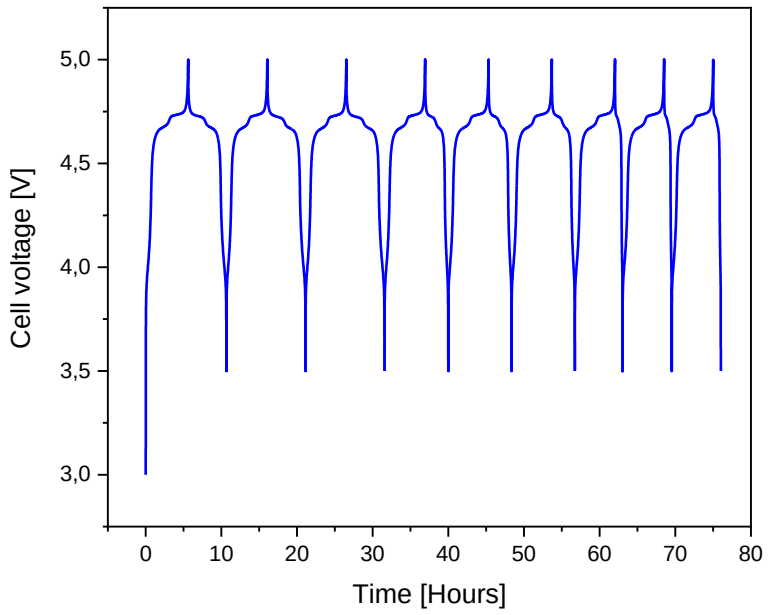

Figure 29 – Galvanostatic charge-discharge profile at C/5, C/3, and C/1 discharge rate of the K-LMNO cathode A11 (charge rate was always C/5 for each cycle).

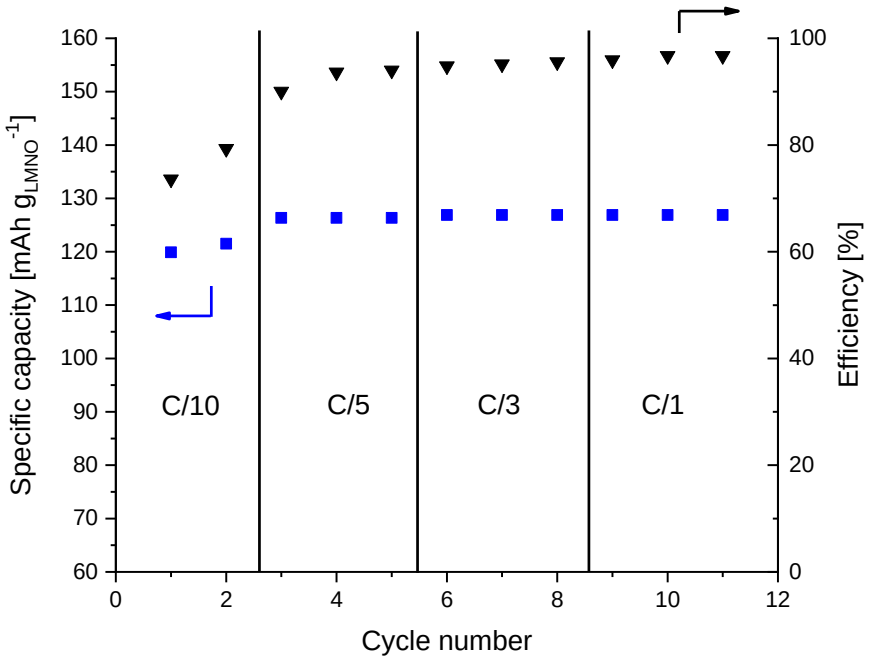

Figure 30 – Discharge capacity normalized to the LMNO mass and coulombic efficiency as a function of cycle number of the K-LMNO cathode A11 with cut-off potentials 3.5 - 5 V vs Li^+/Li.

Table 9 - Discharge current (I), charge (Q_c) and discharge (Q_d) capacities in mAh, discharge capacity normalized to the composite ($Q_{composite}$) and LMNO (Q_{LMNO}) mass loading, and coulombic efficiency (η), for the K-LMNO cathode A11.

Cycle	C-rate	I [mA]	Q_c [mAh]	Q_d [mAh]	$Q_{composite}$ [mAh/g]	Q_{LMNO} [mAh/g]	η [%]
1	C/5	0.047	0.261	0.235	101.29	126.34	90.0
2		0.047	0.251	0.235	101.29	126.34	93.6
3		0.047	0.250	0.235	101.29	126.34	94.0
4	C/3	0.078	0.249	0.236	101.72	126.88	94.8
5		0.078	0.248	0.236	101.72	126.88	95.2
6		0.078	0.247	0.236	101.72	126.88	95.5
7	C/1	0.233	0.246	0.236	101.72	126.88	95.9
8		0.233	0.244	0.236	101.72	126.88	96.7
9		0.233	0.244	0.236	101.72	126.88	96.7

Figure 31 shows the trend of the capacity as a function of the cycle number during the life stability test run at C/1 (both for charge and discharge). Figure 32 compares the voltage profile of 1st and 70th cycle. Unfortunately, the test was stopped only after 70 cycles due to an internal blackout of the building that occurred in those days.

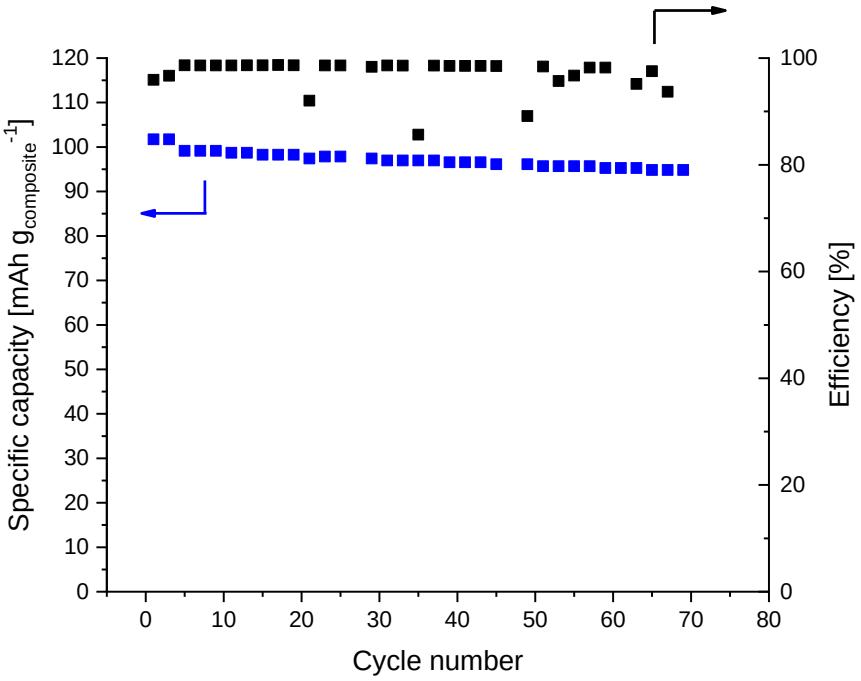

Figure 31 – Trend of discharge capacity normalized to the composite mass over 70 cycles carried out at C/1 (both for charge and discharge) of the K-LMNO cathode A11 with cut-off potentials 3.5 - 5 V vs Li^+/Li.

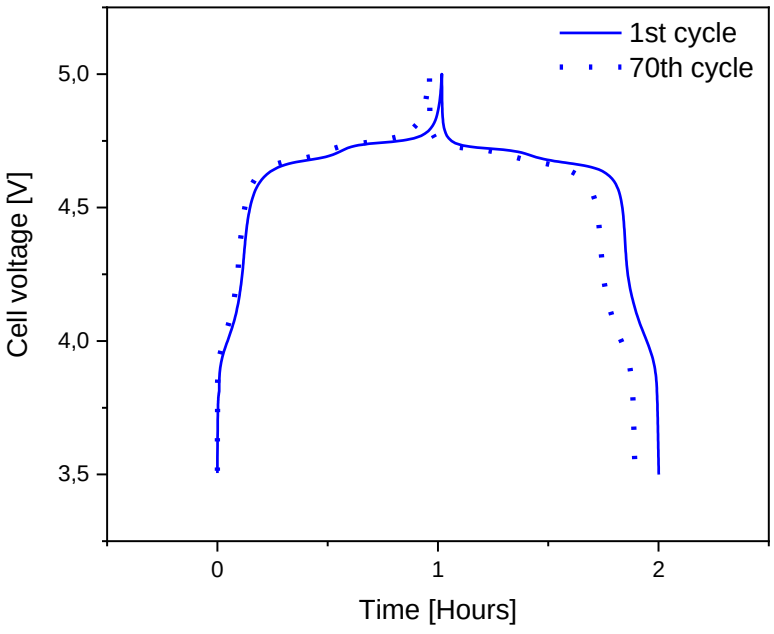

Figure 32 – Galvanostatic charge-discharge profile at C/1 at 1st and 70th cycle of the K-LMNO cathode A11.

Table 10 reports the data evaluated by the cycle-life stability test. The capacity fading was going quite well since the cell lost ca. 5% in 70 cycles.

Table 10 - Charge and discharge current (I), charge (Q_c) and discharge (Q_d) capacities in mAh, discharge capacity normalized to the composite ($Q_{composite}$) and LMNO (Q_{LMNO}) mass loading, and coulombic efficiency (η) of the K-LMNO cathode A11.

Cycle	I [mA]	Q_c [mAh]	Q_d [mAh]	$Q_{composite}$ [mAh/g]	Q_{LMNO} [mAh/g]	η [%]
1	± 0.233	0.233	0.231	99.6	124.2	99.1
2	± 0.233	0.234	0.230	99.1	123.7	98.3
3	± 0.233	0.233	0.230	99.1	123.7	98.7
68	± 0.233	0.234	0.217	93.5	116.7	92.7
69	± 0.233	0.299	0.209	90.1	112.4	69.9
70	± 0.233	0.222	0.219	94.4	117.7	98.6

3.1.1.3 Pressure trend investigation

It often happened that the first CVs cycle of some electrodes tested in Swagelock cells were noisy, like the one depicted in Figure 33, relative to the K-LMNO A13 cathode. For this reason, we decided to investigate the pressure evolution inside the cell adopting the EL-Cell described in Section 2.2.2.

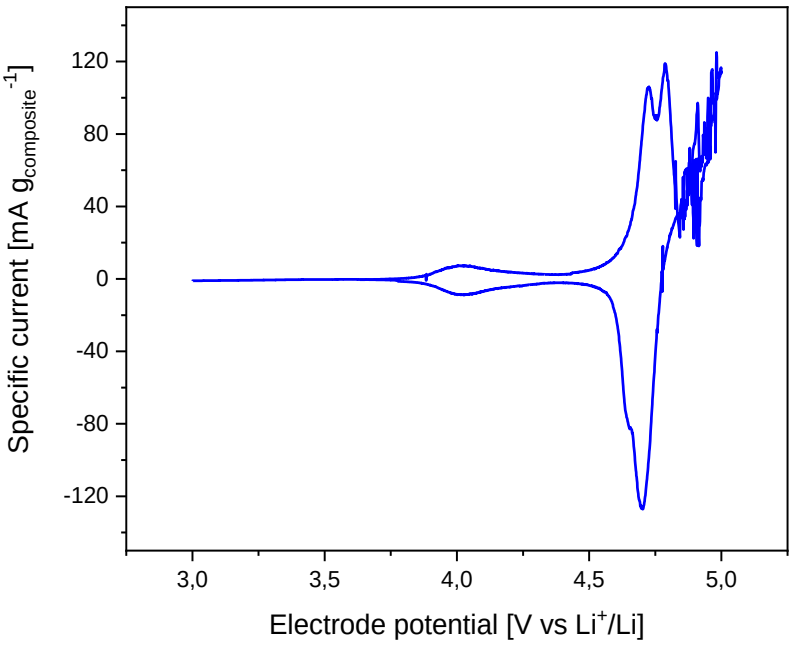

Figure 33 – Cyclic voltammetry of K-LMNO cathode A13 at 50 µV/s normalized to the composite current.

The EL-Cell cell assembled featured the so called A16 cathode, metallic lithium as counter electrode, Whatman GF/F as separator, and LP30 as electrolyte. It was a 2-electrode cell: the lithium foil was simultaneously used as counter and reference electrode. We only performed three cyclic voltammetry at 50 µV/s while monitoring the pressure evolution with the PAT-Press-Box. Figure 34 depicts the CVs profile, with current normalized to the composite cathode mass. Figure 35 shows the pressure trend and electrode potential as a function of time during the test. It can be seen that the first cycle is not noisy like the one in Figure 33, and the peaks for the three redox reactions partially overlap as expected to occur. The pressure increases of ca. 12% is due to the gas formation inside the cell during the formation of the CEI in the first cycles.

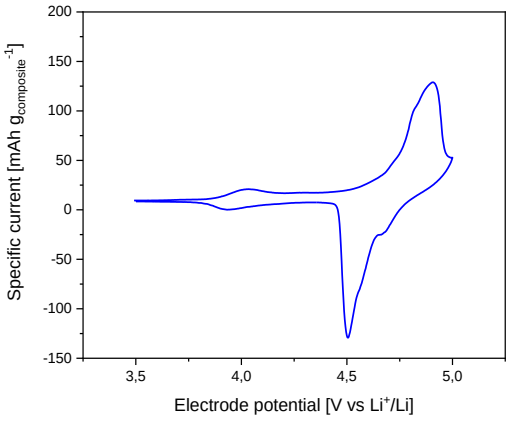

a)

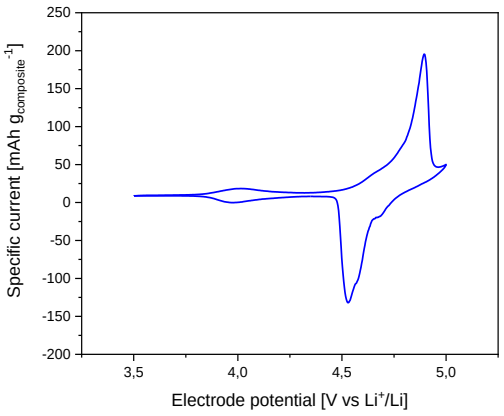

b)

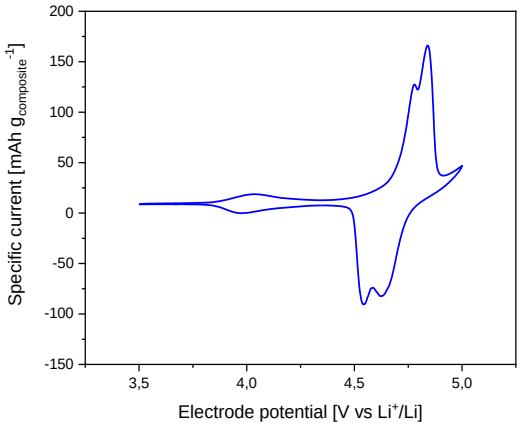

c)

Figure 34 – Cyclic voltammogram of K-LMNO A16 in EL-Cell at 50 µV/s normalized to the composite current of the a) first cycle, b) second cycle, and c) third cycle.

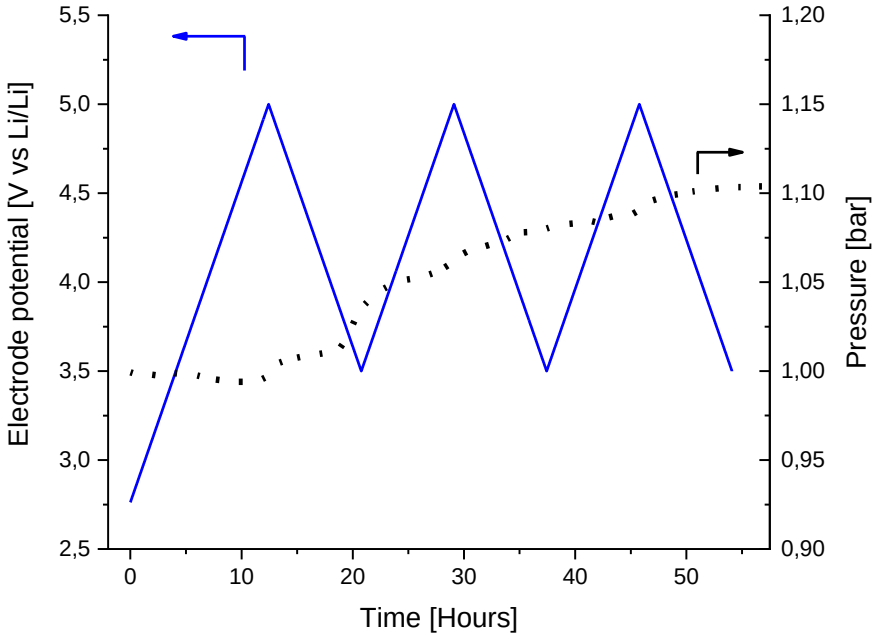

Figure 35 – Pressure trend and electrode potential as a function of time of the K-LMNO cathode A16 in EL-Cell.

3.1.2 S-LMNO1

3.1.2.1 S-LMNO1 electrode preparation

Initially, Solef PVDF was dissolved in NMP by stirring overnight. Then, the binder solution was added in a jar with LMNO and C65 powders for the ball milling process at 300 rpm for 90 + 90 (reverse) minutes. The obtained slurry was casted on the aluminium current collector. The coated film was dried at RT over the night, then for few hours at 80°C in a thermostatic oven before cutting and pressing at 2 Ton/cm^2, and dried again under dynamic vacuum (BUCHI oven) for 12 hours at 120°C to eliminate any trace of NMP. The final composition of the S-LMNO1 cathodes was: 80% LMNO, 10% C65, 10% Solef PVDF.

With this formulation 5 electrodes were prepared with the total (including aluminum), composite and LMNO loadings reported in Table 11. Electrodes A31, A32, A33 and A34 were tested in Bola cell but in following section 3.1.2.2 will be reported the data about the A31 electrode.

Table 11 – Code, total (including aluminium foil), post vacuum heating, composite and LMNO masses of the S-LMNO1 electrodes.

Electrode's code	Mass post vacuum heating [mg]	Composite mass [mg]	LMNO mass [mg]
A31	6.01	3.21	2.57
A32	5.32	2.52	2.02
A33	4.99	2.19	1.75
A34	5.97	3.17	2.54
A35	4.62	1.82	1.46

3.1.2.2 S-LMNO1 electrode electrochemical tests

Figure 36 shows the electrode potential profiles during the conditioning galvanostatic charge-discharge at C/10. Figure 37 reports the charge and discharge curves as a function of the composite specific capacity and in Figure 38 the differential capacity profile. Table 12 reports the charge and discharge electrode capacities in mAh, as well as the specific capacity values normalized to the composite and LMNO mass, and the coulombic efficiency evaluated by this test.

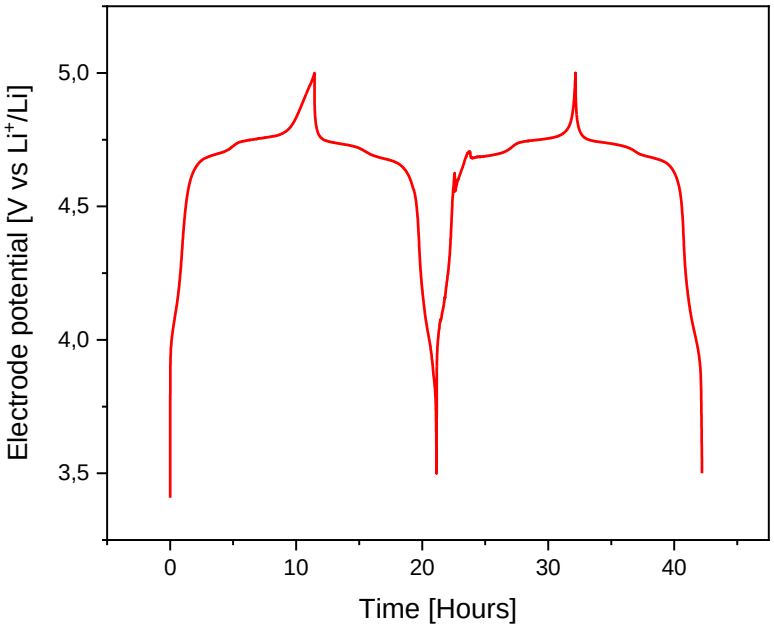

Figure 36 – Electrode potential profiles as function of time of the two conditioning cycles at C/10 of the S-LMNO1 cathode A31.

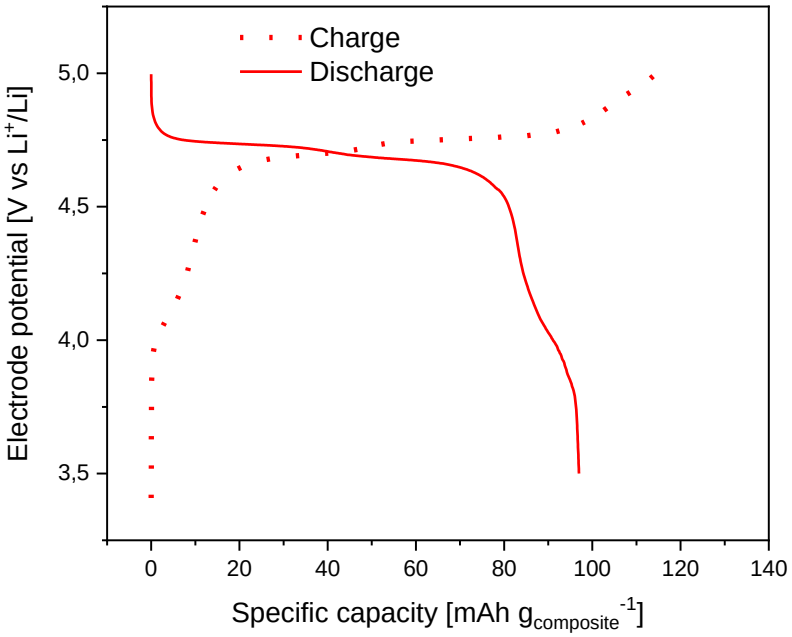

Figure 37 - Charge and discharge curves of the first cycle at C/10 as a function of the cycled composite capacity of the S-LMNO1 cathode A31.

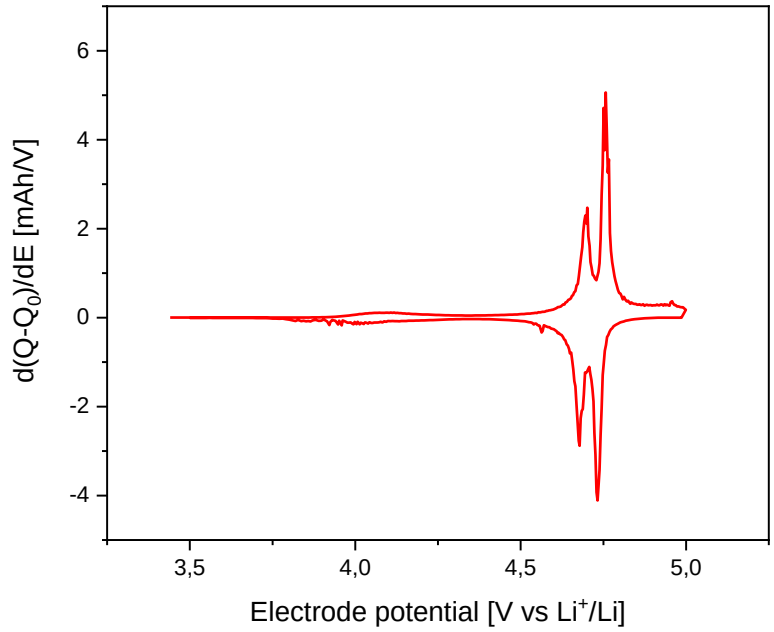

Figure 38 - Differential profile of d(Q-Q0)/dE of the first galvanostatic charge-discharge cycle at C/10 of the S-LMNO1 cathode A31.

Table 12 - Charge and discharge current (I), charge (Q_c) and discharge (Q_d) capacities in mAh, discharge capacity normalized to the composite ($Q_{composite}$) or LMNO (Q_{LMNO}) mass loading, and coulombic efficiency (η) evaluated from the conditioning cycles of the S-LMNO1 cathode A31..

Cycle	I [mA]	Q_c [mAh]	Q_d [mAh]	$Q_{composite}$ [mAh/g]	Q_{LMNO} [mAh/g]	η [%]
1	± 0.032	0.367	0.311	96.9	121.0	84.7
2	± 0.032	0.354	0.322	100.3	125.3	91.0

Figure 39 depicts the CV profile normalized to the composite current. The peaks are not as sharp as in the CV of Figure 28. This might be due to the fact that the S-LMNO1 cathode A31 features a composite mass loading of 3,21 mg, that his higher than that of K-LMNO electrodes (A11 2,32 mg). Indeed, it is well known that the electrode response much depends on the thickness of the composite layer. The increase of the areal mass loading and thickness hinders electron connection

and ion access through the bulk electrode. Consequently, not all the material is exploited with the same efficacy.

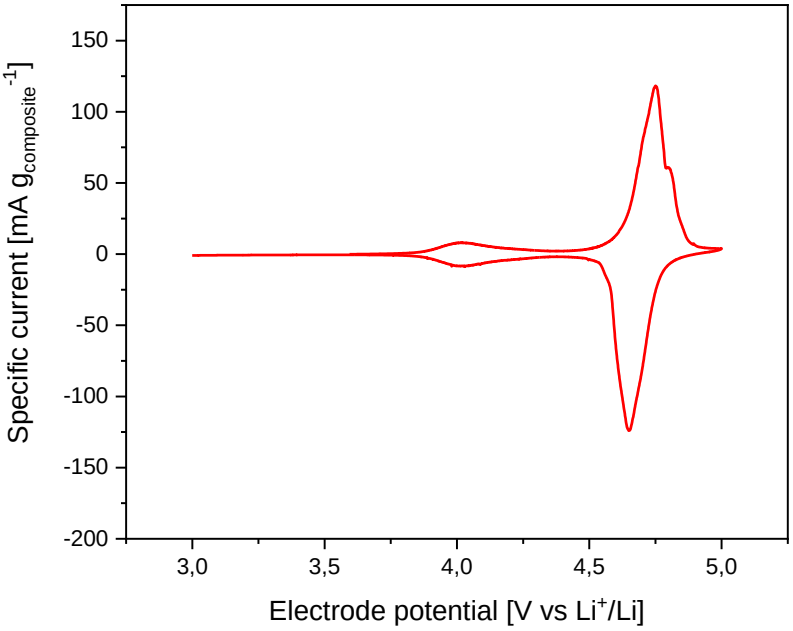

Figure 39 - Cyclic voltammetry of S-LMNO1 A31 cathode at 50 µV/s normalized to the composite current.

After that, the rate capability test has been carried out. Figure 40 and Figure 41 show the electrode potential profiles at each C-rate, and the specific LMNO capacity and efficiency as a function of the cycle number, respectively. Table 13 reports the data evaluated by this test. The cell showed a great capacity retention with the same discharge capacity despite the increasing of the discharge current. Also, the specific LMNO capacity values agree with the capacity claimed by the LMNO manufacturer of 125 mAh/g.

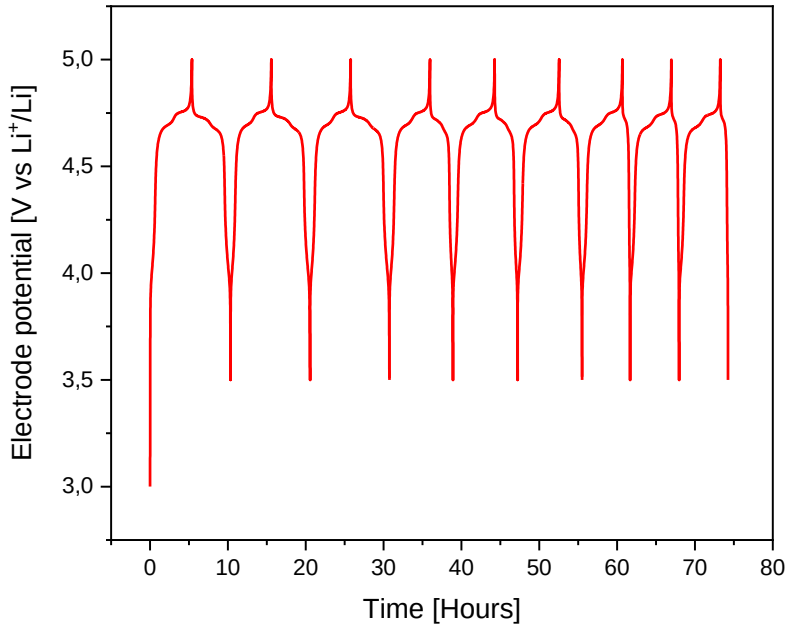

Figure 40 - Galvanostatic charge-discharge profile at C/5, C/3, and C/1 discharge rate of the S-LMNO1 cathode A31 (charge at C/5 for all the discharge rates).

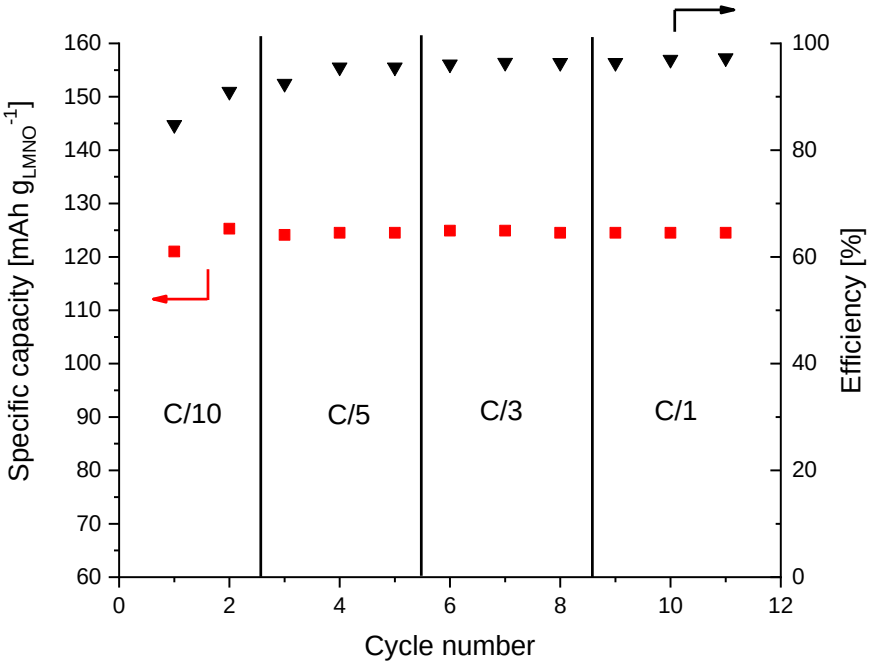

Figure 41 - Discharge capacity normalized to the LMNO mass and coulombic efficiency as a function of cycle number of the S-LMNO1 cathode A31 with cut-off potentials 3.5 - 5 V vs Li^+/Li.

Table 13 - Discharge current (I), charge (Q_c) and discharge (Q_d) capacities in mAh, discharge capacity normalized to the composite ($Q_{composite}$) and LMNO (Q_{LMNO}) mass loading, and coulombic efficiency (η) of the S-LMNO1 cathode A31.

Cycle	C-rate	I [mA]	Q_c [mAh]	Q_d [mAh]	$Q_{composite}$ [mAh/g]	Q_{LMNO} [mAh/g]	η [%]
1	C/5	0.064	0.345	0.319	99.4	124.1	92.5
2		0.064	0.335	0.320	99.7	124.5	95.5
3		0.064	0.335	0.320	99.7	124.5	95.5
4	C/3	0.107	0.334	0.321	100.0	124.9	96.1
5		0.107	0.333	0.321	100.0	124.9	96.4
6		0.107	0.332	0.320	99.7	124.5	96.4
7	C/1	0.321	0.332	0.320	99.7	124.5	96.4
8		0.321	0.330	0.320	99.7	124.5	97.0
9		0.321	0.329	0.320	99.7	124.5	97.3

We concluded with life stability test performed with 1C charge and discharge current for over 180 cycles. In Figure 42 and Figure 43 depict the specific capacity trend with cycles number and the comparison between the electrode potential profile of the 1st and 180th cycle, respectively. Table 14 reports the data collected by this test. The cell lost ca. 23% of the initial capacity over 180 cycles.

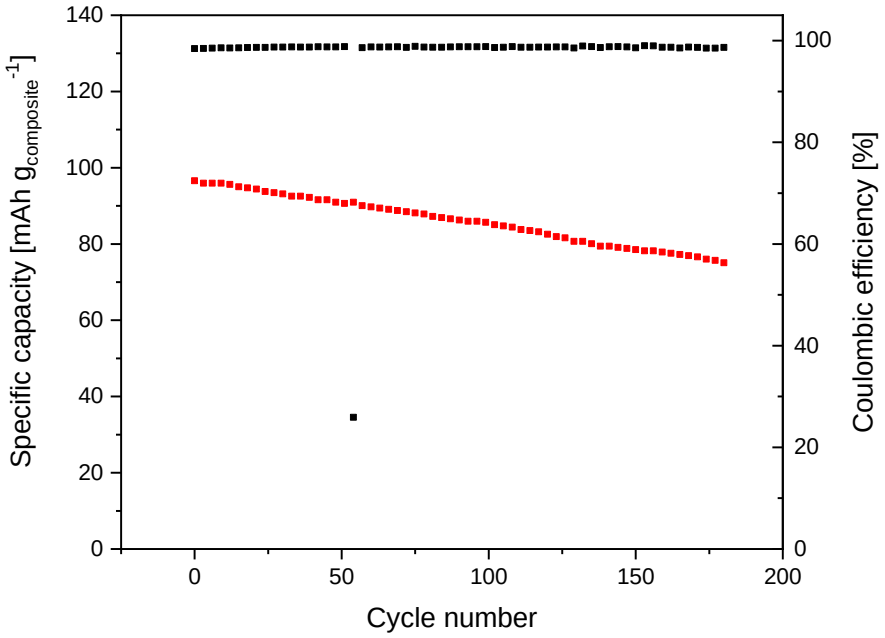

Figure 42 - Trend of discharge capacity normalized to the composite mass over 180 cycles at C/1 (charge and discharge) of the S-LMNO1 cathode A31 with cut-off potentials 3.5 - 5 V vs Li^+/Li.

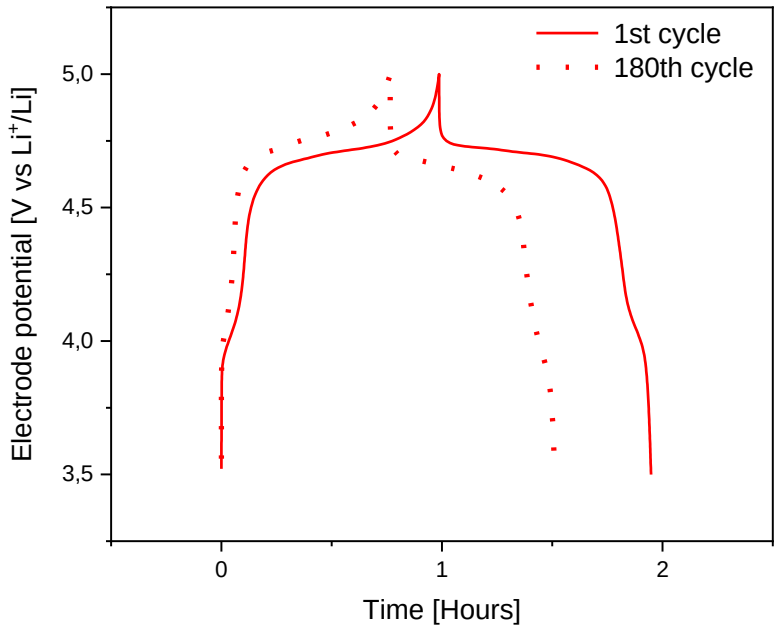

Figure 43 - Galvanostatic charge-discharge profile at C/1 at 1st and 180th cycle of the S-LMNO1 cathode A31.

Table 14 - Charge and discharge current (I), charge (Q_c) and discharge (Q_d) capacities in mAh, discharge capacity normalized to the composite ($Q_{composite}$) and LMNO (Q_{LMNO}) mass loading, and coulombic efficiency (η) of the S-LMNO1 cathode A31.

Cycle	I [mA]	Q_c [mAh]	Q_d [mAh]	$Q_{composite}$ [mAh/g]	Q_{LMNO} [mAh/g]	η [%]
1	± 0.321	0.315	0.310	96.6	120.6	98.4
2	± 0.321	0.315	0.310	96.6	120.6	98.4
3	± 0.321	0.314	0.309	96.3	120.2	98.4
178	± 0.321	0.246	0.242	75.4	94.2	98.4
179	± 0.321	0.245	0.242	75.4	94.2	98.8
180	± 0.321	0.244	0.241	75.1	93.8	98.8

3.1.3 S-LMNO2

3.1.3.1 S-LMNO2 electrode preparation

Initially, Solef PVDF was dissolved in NMP by stirring overnight. Then, the binder solution was added in a jar with LMNO and C65 powders for the ball milling process at 300 rpm for 90 + 90 (reverse) minutes. The obtained slurry was coated on the aluminium current collector. The coated film was dried at RT for 5 days due to an emergency close of the department, then overnight at 80°C in a thermostatic oven before cutting and pressing at 2 Ton/cm^2, and dried again under dynamic vacuum (BUCHI oven) for 12 hours at 120°C to eliminate any trace of NMP. The final composition of the K-LMNO cathodes was: 90% LMNO, 5% C65, 5% Kynar PVDF.

With this formulation 5 electrodes were prepared with the total (including aluminum), composite and LMNO loadings reported Table 15. In Section 3.1.3.2 will be reported the data about the A41 electrode.

Table 15 – Code, total (including aluminium foil), post vacuum heating, composite and LMNO masses of s of the S-LMNO2 electrodes.

Electrode's code	Mass post vacuum heating [mg]	Composite mass [mg]	LMNO mass [mg]
A41	4.42	1.56	1.40
A42	3.66	0.80	0.72
A43	3.46	0.60	0.54
A44	3.81	0.95	0.85
A45	3.47	0.61	0.55

3.1.3.2 S-LMNO2 electrode electrochemical test

The galvanostatic profile at C/10, the differential capacity and the CV, normalized to the composite current are shown in Figure 44, Figure 45, Figure 46 and Figure 47. Table 16 reports the capacity data obtained by the analysis of the galvanostatic test at C/10. For this cell only one C/10 cycle was performed.

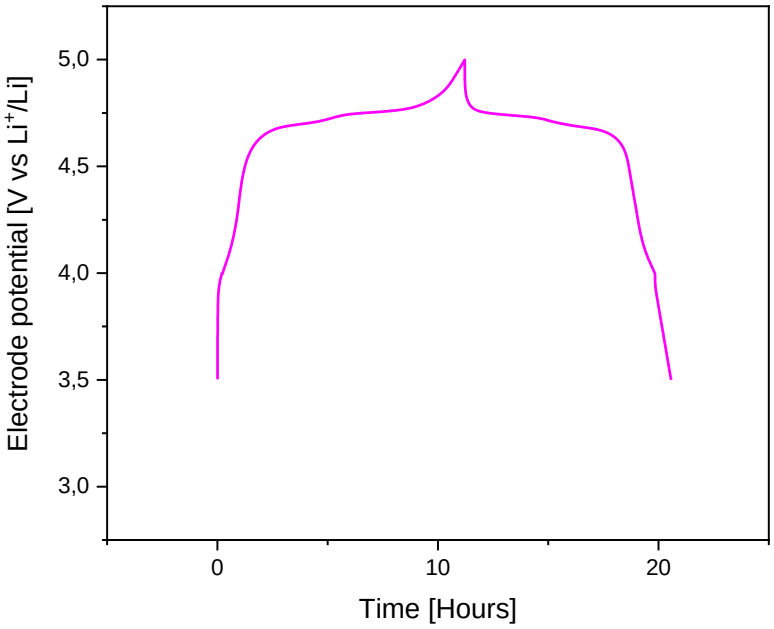

Figure 44 – Electrode potential profile as function of time of the conditioning cycle at C/10 of the S-LMNO2 cathode A41.

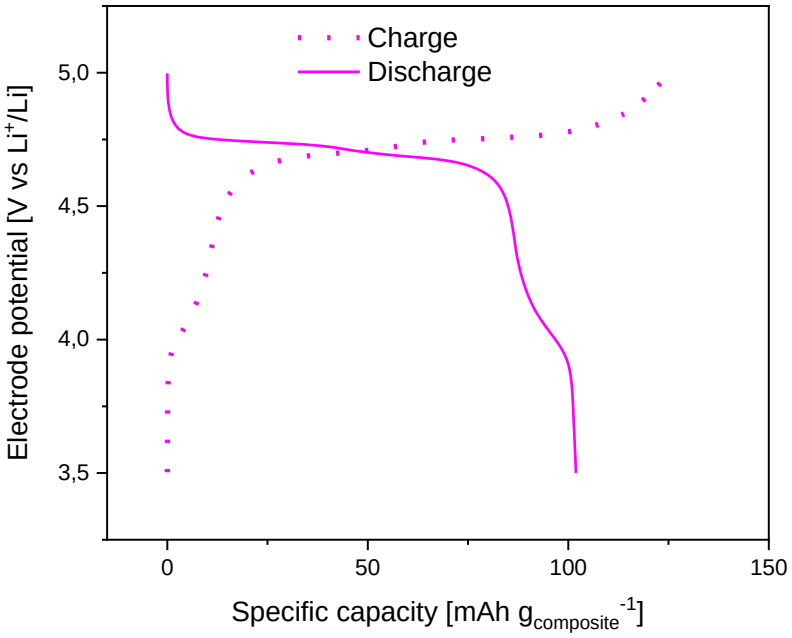

Figure 45 - Charge and discharge curves of the first cycle at C/10 as a function of the cycled composite capacity of the S-LMNO2 cathode A41.

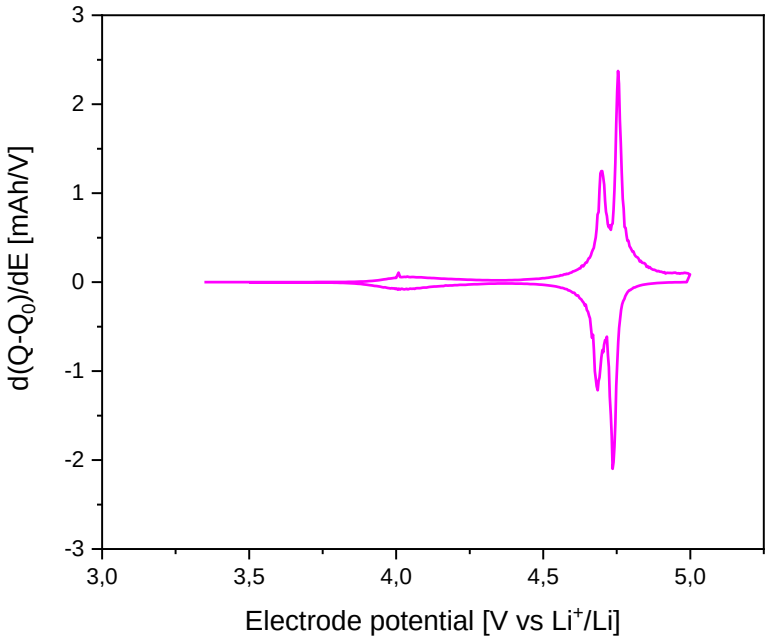

Figure 46 – Differential profile of d(Q-Q0)/dE of the first galvanostatic charge-discharge cycle at C/10 of the S-LMNO2 cathode A41.

Table 16 - Charge and discharge current (I), charge (Q_c) and discharge (Q_d) capacities in mAh, discharge capacity normalized to the composite ($Q_{composite}$) or LMNO (Q_{LMNO}) mass loading, and coulombic efficiency (η) evaluated from the conditioning cycles of the S-LMNO2 cathode A41..

Cycle	I [mA]	Q_c [mAh]	Q_d [mAh]	$Q_{composite}$ [mAh/g]	Q_{LMNO} [mAh/g]	η [%]
1	± 0.017	0.196	0.159	101.9	113.6	81.1

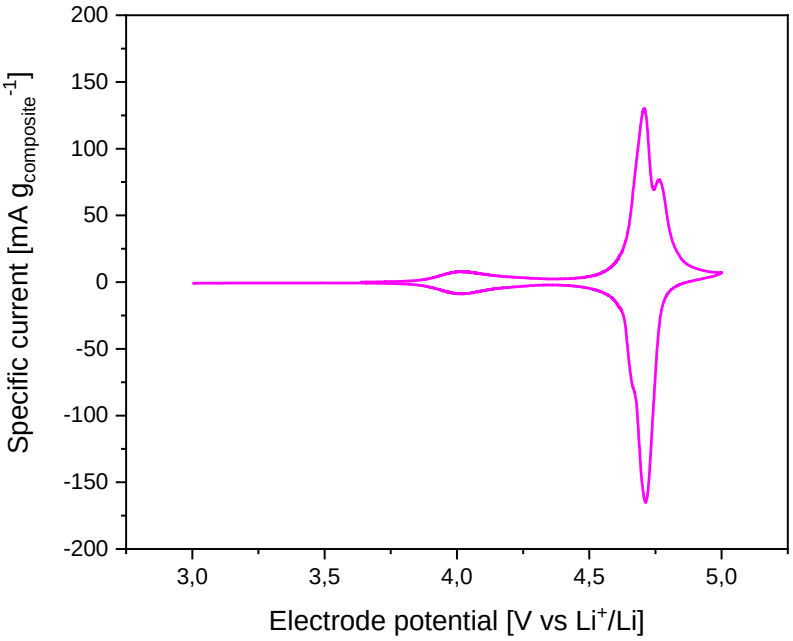

Figure 47 - Cyclic voltammetry of S-LMNO2 cathode A41 at 50 µV/s normalized to the composite current.

After conditioning, the capability rate has been carried out. Figure 48 reports the discharge profiles at different C-rates (C/5, C/3 and C/1). For each cycle, the charge was done at C/5. Figure 49 shows the discharge capacity normalized to the active material mass in function of the number of cycles, as well as the coulombic efficiency of each cycle. The capacity and coulombic efficiency delivered at each C-rates are reported in Table 17. The electrode shows a good capacity retention with only a ca. 3% decrease from C/5 to C/1.

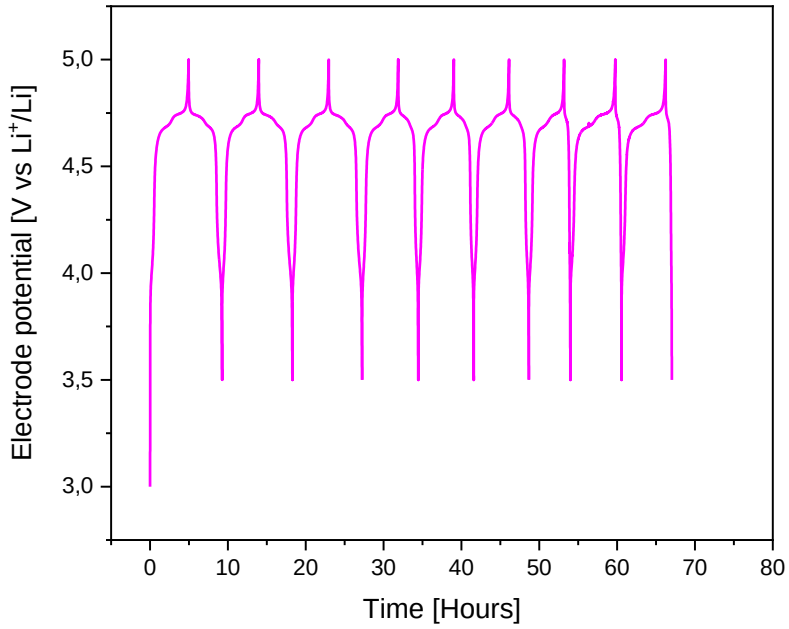

Figure 48 – Galvanostatic charge-discharge profile at C/5, C/3, and C/1 discharge rate of the S-LMNO2 cathode A41.

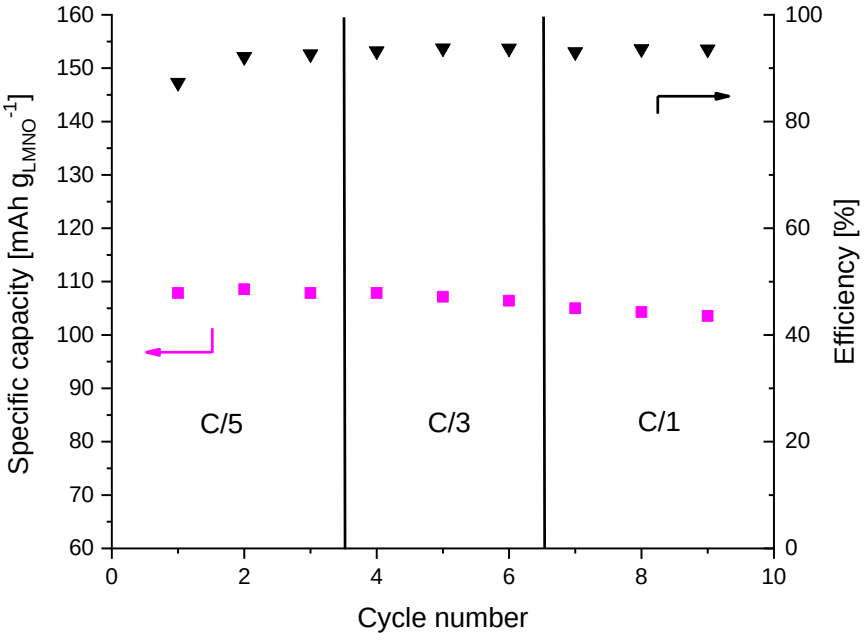

Figure 49 - Discharge capacity normalized to the LMNO mass and coulombic efficiency as a function of cycle number of the S-LMNO2 cathode A41 with cut-off potentials 3.5 - 5 V vs Li^+/Li.

Table 17 - Discharge current (I), charge (Q_c) and discharge (Q_d) capacities in mAh, discharge capacity normalized to the composite ($Q_{composite}$) and LMNO (Q_{LMNO}) mass loading, and coulombic efficiency (η) of the S-LMNO2 cathode A41..

Cycle	C-rate	I [mA]	Q_c [mAh]	Q_d [mAh]	$Q_{composite}$ [mAh/g]	Q_{LMNO} [mAh/g]	η [%]
1	C/5	0.035	0.173	0.151	96.8	107.8	87.3
2		0.035	0.165	0.152	97.4	108.6	92.1
3		0.035	0.163	0.151	96.8	107.8	92.6
4	C/3	0.058	0.162	0.151	96.8	107.8	93.2
5		0.058	0.160	0.150	96.2	107.1	93.7
6		0.058	0.159	0.149	95.5	106.4	93.7
7	C/1	0.175	0.158	0.147	94.2	105.0	93.0
8		0.175	0.156	0.146	93.6	104.3	93.6
9		0.175	0.155	0.145	92.9	103.6	93.5

The trend of specific capacity vs cycle number at C/1 (both for the charge and discharge) is shown in Figure 50. Figure 51 compares galvanostatic profiles at C/1 of the 1st and 170th cycle. The specific capacity decreases by 32% over the first 170 cycles as can be seen in Table 18.

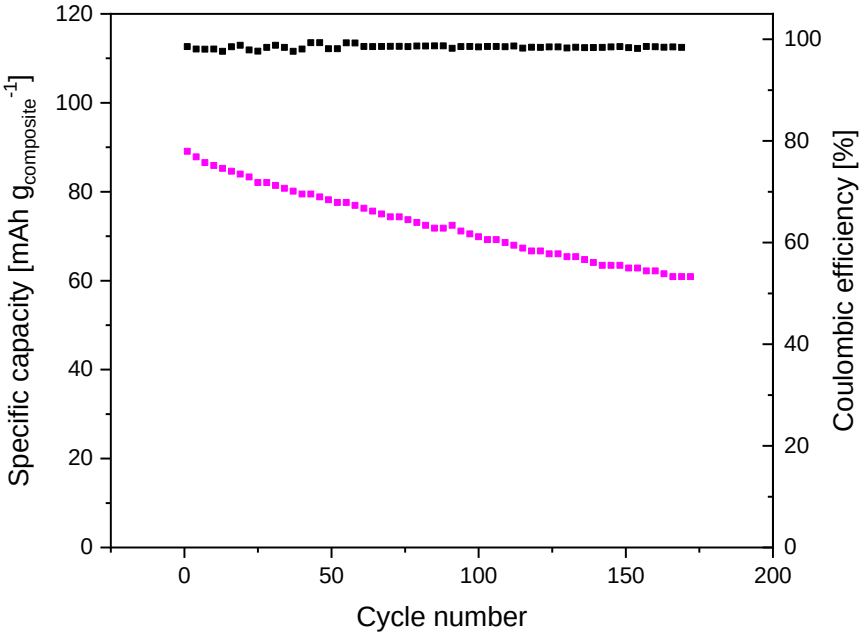

Figure 50 - Trend of discharge capacity normalized to the composite mass and coulombic efficiency over 170 cycles of the S-LMNO2 cathode A41 with cut-off potentials 3.5 - 5 V vs Li^+/Li.

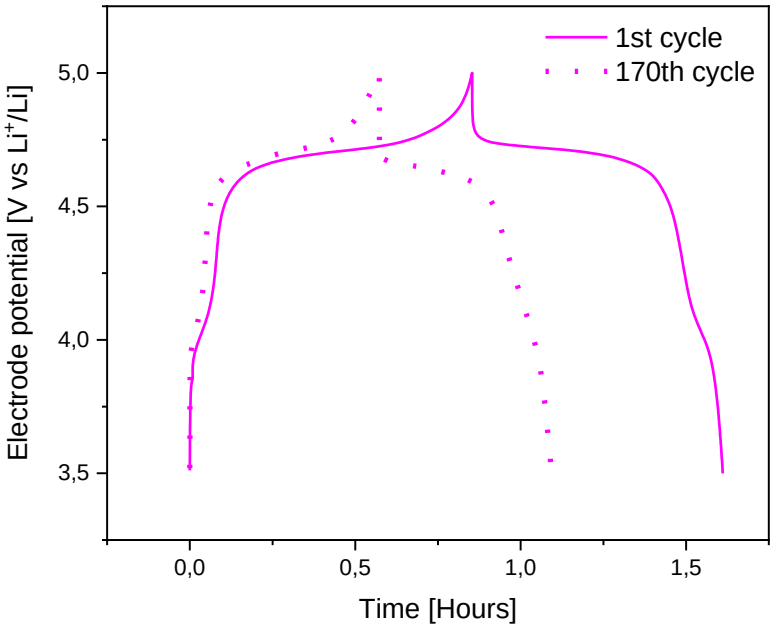

Figure 51 - Galvanostatic charge-discharge profile at C/1 at 1st and 170th cycle of the S-LMNO2 cathode A41.

.

Table 18 - Charge and discharge current (I), charge (Q_c) and discharge (Q_d) capacities in mAh, discharge capacity normalized to the composite ($Q_{composite}$) and LMNO (Q_{LMNO}) mass loading, and coulombic efficiency (η) of the S-LMNO2 cathode A41.

Cycle	I [mA]	Q_c [mAh]	Q_d [mAh]	$Q_{composite}$ [mAh/g]	Q_{LMNO} [mAh/g]	η [%]
1	± 0.175	0.141	0.139	89.1	99.3	98.6
2	± 0.175	0.141	0.138	88.5	98.6	97.9
3	± 0.175	0.140	0.138	88.5	98.6	98.6
168	± 0.175	0.096	0.095	60.9	67.8	98.9
169	± 0.175	0.096	0.095	60.9	67.8	98.9
170	± 0.175	0.096	0.094	60.2	67.1	97.9

3.1.4 S-LMNO3

3.1.4.1 S-LMNO3 electrode preparation

Initially, Solef PVDF was dissolved in NMP by stirring overnight. Then, the binder solution was added in a jar with LMNO and C65 powders for the ball milling process at 300 rpm for 90 + 90 (reverse) minutes. The obtained slurry was casted on the aluminium current collector. The coated film was dried at RT for 5 days due to an emergency close of the department, then overnight at 80°C in a thermostatic oven before cutting and pressing at 2 Ton/cm^2, and dried again under dynamic vacuum (BUCHI oven) for 12 hours at 120°C to eliminate any trace of NMP. The final composition of the K-LMNO cathodes was: 85% LMNO, 7.5% C65, 7.5% Kynar PVDF.

With this formulation 5 electrodes were prepared with the total (including aluminum), composite and LMNO loadings reported in Table 19. Electrodes A53 were tested in Bola cell and in following section 3.1.4.2 will be reported the results of its characterization.

Table 19 – Code, total (including aluminium foil), post vacuum heating, composite and LMNO masses of the S-LMNO3 electrodes.

Electrode's code	Mass post vacuum heating [mg]	Composite mass [mg]	LMNO mass [mg]
A51	4.99	2.08	1.77
A52	5.00	2.09	1.78
A53	5.04	2.13	1.81
A54	5.10	2.19	1.86
A55	5.15	2.24	1.90

3.1.4.2 S-LMNO3 electrode electrochemical tests

Figure 52 and Figure 53 shown the conditioning galvanostatic profile at C/10. Figure 54 depicts the differential capacity profile. Table 20 reports the charge and discharge electrode capacities in mAh, as well as the specific capacity values normalized to the composite and LMNO mass, and the coulombic efficiency evaluated by this test.

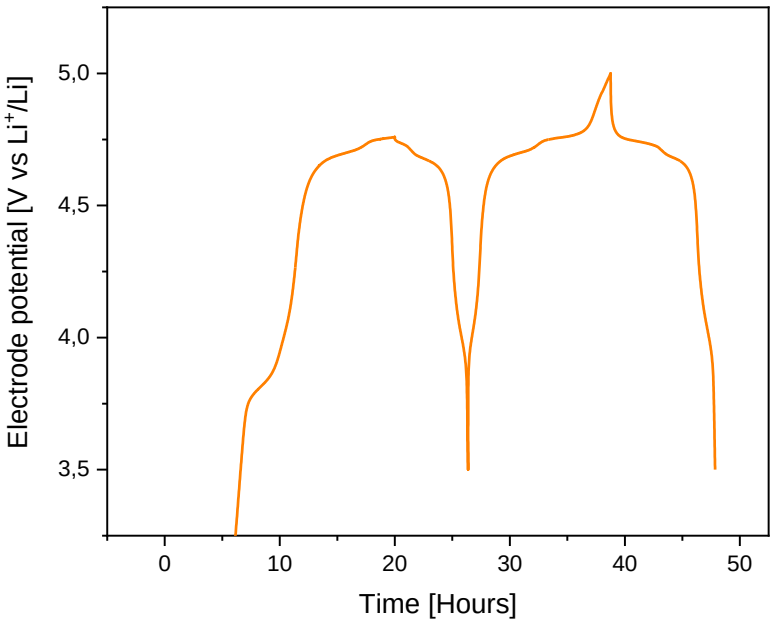

Figure 52 – Electrode potential profile as function of time of the conditioning cycles at C/10 of the S-LMNO3 cathode A53.

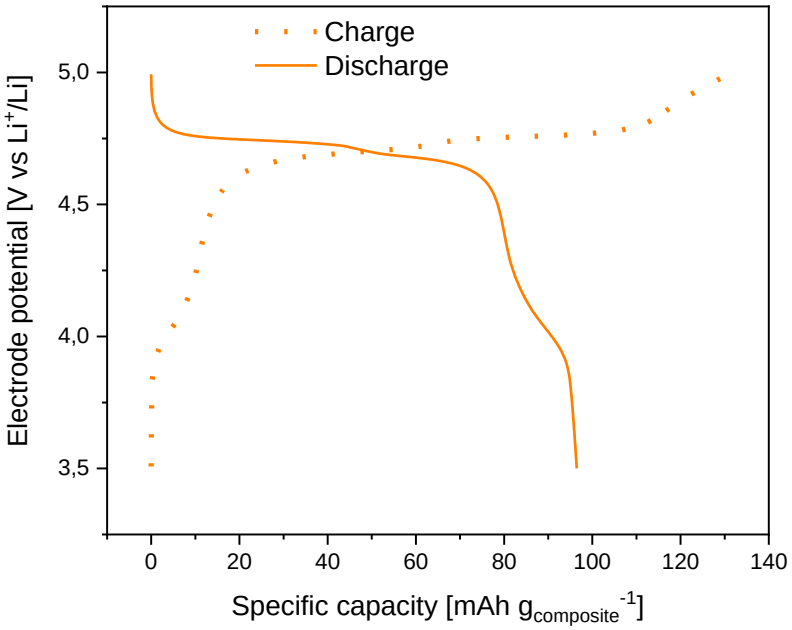

Figure 53 – Charge and discharge curves of the second cycle at C/10 as a function of the cycled composite capacity of the S-LMNO3 cathode A53.

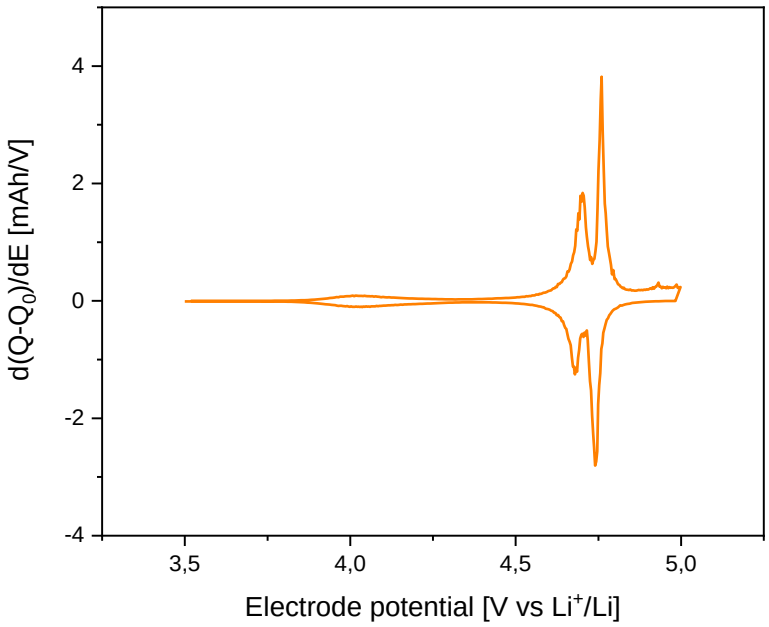

Figure 54 - Differential profile of d(Q-Q0)/dE of the second galvanostatic charge-discharge cycle at C/10 of the S-LMNO3 cathode A53.

Table 20 - Charge and discharge current (I), charge (Q_c) and discharge (Q_d) capacities in mAh, discharge capacity normalized to the composite ($Q_{composite}$) or LMNO (Q_{LMNO}) mass loading, and coulombic efficiency (η) evaluated from the conditioning cycles of the S-LMNO1 cathode A31.

Cycle	I [mA]	Q_c [mAh]	Q_d [mAh]	$Q_{composite}$ [mAh/g]	Q_{LMNO} [mAh/g]	η [%]
1	± 0.023	0.453	0.144	67.6	79.5	31.8
2	± 0.023	0.280	0.205	96.2	113.2	73.2

After conditioning, we performed two cyclic voltammetry and Figure 55 depicts the 2nd cycle.

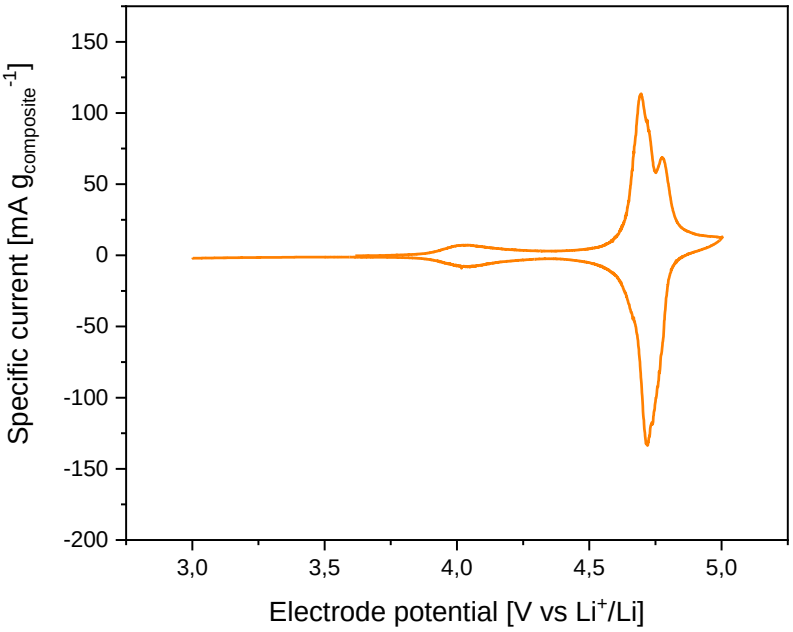

Figure 55 - Cyclic voltammetry of S-LMNO3 cathode A53 at 50 µV/s normalized to the composite current.

After conditioning, the capability rate test has been carried out. Figure 56 reports the discharge profiles at different C-rates (C/5, C/3 and C/1). For each cycle, the charge was done at C/5. Figure 57 shows the discharge capacity normalized to the active material mass in function of the number of cycles, as well as the coulombic efficiency of each cycle. The capacity and coulombic efficiency delivered at each C-rates are reported in Table 21. Even this electrode showed a good capacity retention with a small decrease only in increasing from C/3 to C/1.

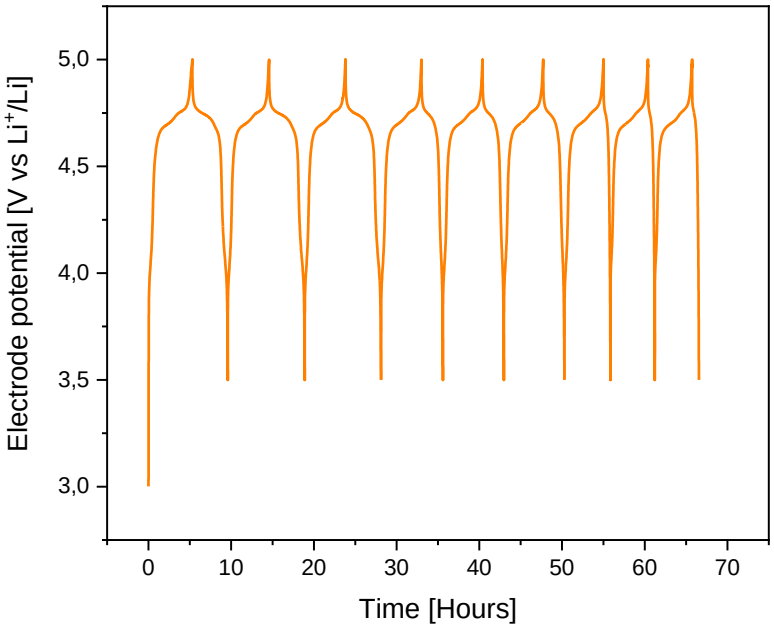

Figure 56 – Galvanostatic charge-discharge profile at C/5, C/3, and C/1 discharge rate of the S-LMNO3 cathode A53.

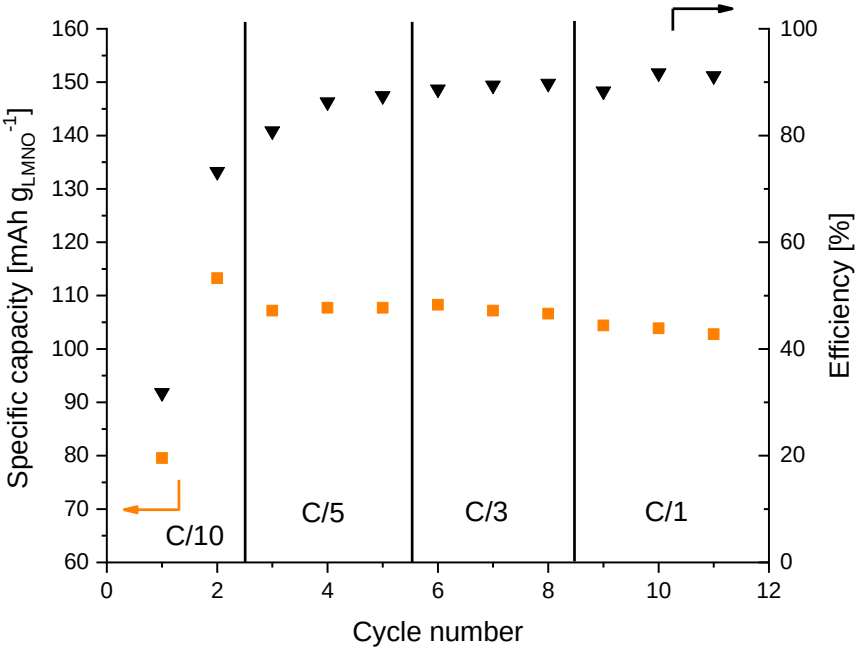

Figure 57 - Discharge capacity normalized to the LMNO mass and coulombic efficiency as a function of cycle number of the S-LMNO3 cathode A53 with cut-off potentials 3.5 - 5 V vs Li^+/Li.

Table 21 - Discharge current (I), charge (Q_c) and discharge (Q_d) capacities in mAh, discharge capacity normalized to the composite ($Q_{composite}$) and LMNO (Q_{LMNO}) mass loading, and coulombic efficiency (η) of the S-LMNO3 cathode A53.

Cycle	C-rate	I [mA]	Q_c [mAh]	Q_d [mAh]	$Q_{composite}$ [mAh/g]	Q_{LMNO} [mAh/g]	η [%]
1	C/5	0.045	0.240	0.194	91.1	107.2	80.8
2		0.045	0.226	0.195	91.5	107.7	86.3
3		0.045	0.223	0.195	91.5	107.7	87.4
4	C/3	0.075	0.221	0.196	92.0	108.3	88.7
5		0.075	0.217	0.194	91.1	107.2	89.4
6		0.075	0.215	0.193	90.6	106.6	89.8
7	C/1	0.226	0.214	0.189	88.7	104.4	88.3
8		0.226	0.205	0.188	88.3	103.9	91.7
9		0.226	0.204	0.186	87.3	102.8	91.2

Life stability was the last test to be carried out. Figure 58 shows the capacity trend in function of the number of cycles, as well as the coulombic efficiency of each cycle. Figure 59 compares the 1st and 130th electrode potential profile. Table 22 reports the data evaluated by this test and the electrode showed a loss of capacity of about 50% in 130 cycles.

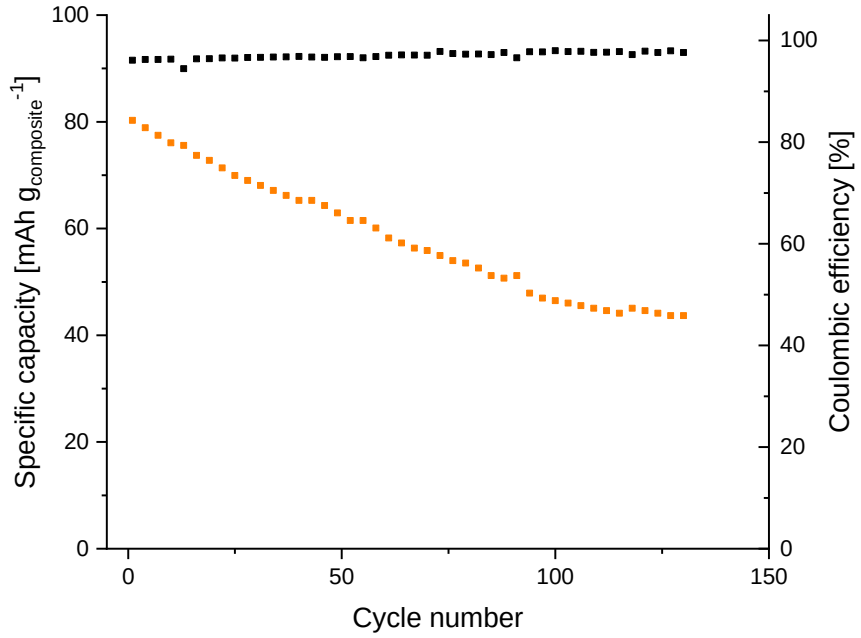

Figure 58 - Trend of discharge capacity normalized to the composite mass and coulombic efficiency over 130 cycles of the S-LMNO3 cathode A53 with cut-off potentials 3.5 - 5 V vs Li^+/Li.

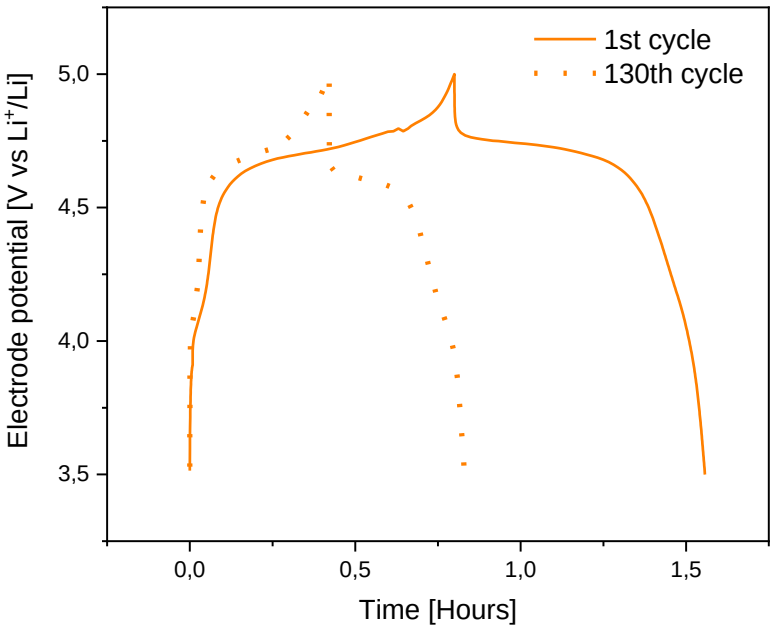

Figure 59 - Galvanostatic charge-discharge profile at C/1 at 1st and 130th cycle of the S-LMNO3 cathode A53.

Table 22 - Charge and discharge current (I), charge (Q_c) and discharge (Q_d) capacities in mAh, discharge capacity normalized to the composite ($Q_{composite}$) and LMNO (Q_{LMNO}) mass loading, and coulombic efficiency (η) of the S-LMNO3 cathode A53.

Cycle	I [mA]	Q_c [mAh]	Q_d [mAh]	$Q_{composite}$ [mAh/g]	Q_{LMNO} [mAh/g]	η [%]
1	± 0.226	0.178	0.171	80.3	94.5	96.1
2	± 0.226	0.177	0.170	79.8	93.9	96.0
3	± 0.226	0.178	0.161	75.6	88.9	90.4
128	± 0.226	0.094	0.092	43.2	50.8	97.9
129	± 0.226	0.096	0.093	43.7	51.4	96.9
130	± 0.226	0.095	0.093	43.7	51.4	97.9

3.2 Comparative data analysis

In this section a comparative analysis of the results presented in previous sections is reported.

Table 23 summarizes the composition and mass loadings of the different electrodes K-LMNO and S-LMNO feature the same mass distribution of the component, but different binder brand. The S-LMNO series feature the same binder but different mass composition. Moving from S-LMNO1 to S-LMNO2 and S-LMNO3 the percentage of LMNO is changed from 80% to 90% and 85 %, while keeping the same binder-to-carbon ratio. This means that binder and carbon content decreases in the order S-LMNO1 > S-LMNO3 > S-LMNO2. The composition was changed in order to understand which formulation could provide the best exploitation of LMNO and gravimetric performance of the composite electrode.

Table 23 – Formulation and electrode code, binder provider, electrode composition, areal composite and LMNO mass loading of the different cathodes.

Code	**Electrode code**	**PVDF provider**	**Composition w/w%**	**Composite areal mass loading**	**LMNO areal mass loading**
K-LMNO	A11	Kynar	80% LMNO 10% PVDF 10% Carbon	3.7 mg cm^{-2}	2.9 mg cm^{-2}
S-LMNO1	A31	Solef	80% LMNO 10% PVDF 10% Carbon	5.1 mg cm^{-2}	4.1 mg cm^{-2}
S-LMNO2	A41	Solef	90% LMNO 5% PVDF 5% Carbon	2.5 mg cm^{-2}	2.2 mg cm^{-2}
S-LMNO3	A53	Solef	85% LMNO 7.5% PVDF 7.5% Carbon	3.4 mg cm^{-2}	2.9 mg cm^{-2}

As first, Figure 60 compares the second voltammetric cycle at 50 μV/s of the tested cathodes.

While the first peak at 4 V, related to the Mn^{3+}/Mn^{4+} redox couple, overlap for the different samples, the main CV waves in the interval from 4.5 V to 5 V are different. Namely, the peak current decrease in the order K-LMNO (3.7 mg/cm^2) > S-LMNO2 (2.5 mg/cm^2) > S-LMNO1 (5.1 mg/cm^2) > S-LMNO3 (3.4 mg/cm^2). The voltammetric discharge capacities follow a different order, being 131 mAh/g_{LMNO} for K-LMNO, 131 mAh/g_{LMNO} for S-LMNO1, 123 mAh/g_{LMNO} for S-LMNO3 and 119 mAh/g_{LMNO} for S-LMNO2.

It should be noted that CVs were considered as a step of the conditioning procedure, hence they only give an indication about the redox processes that are taking place and the preliminary behaviour of the cathodes. However, from Figure 39 it can be argued that:

- the electrodes feature similar electrochemical behaviour.
- electrode thickness affect kinetics and brings about broader CV peaks. This is highlighted by the comparison of the CVs of S-LMNO1 that feature the same binder and carbon content, but different areal mass (3.7 mg/cm^2 for K-LMNO and 5.1 mg/cm^2 for S-LMNO1).
- when a low mass loading is considered, a higher content of carbon is beneficial for the process. Indeed, S-LMNO2 (2.5 mg/cm^2) and S-LMNO3 (3.4 mg/cm^2) that display the 5% and 7.5% of carbon provide broader voltammograms compared to K-LMNO (10% carbon, 3.7 mg/cm^2), which could be related to a worse electronic connection of LMNO compared to the samples.

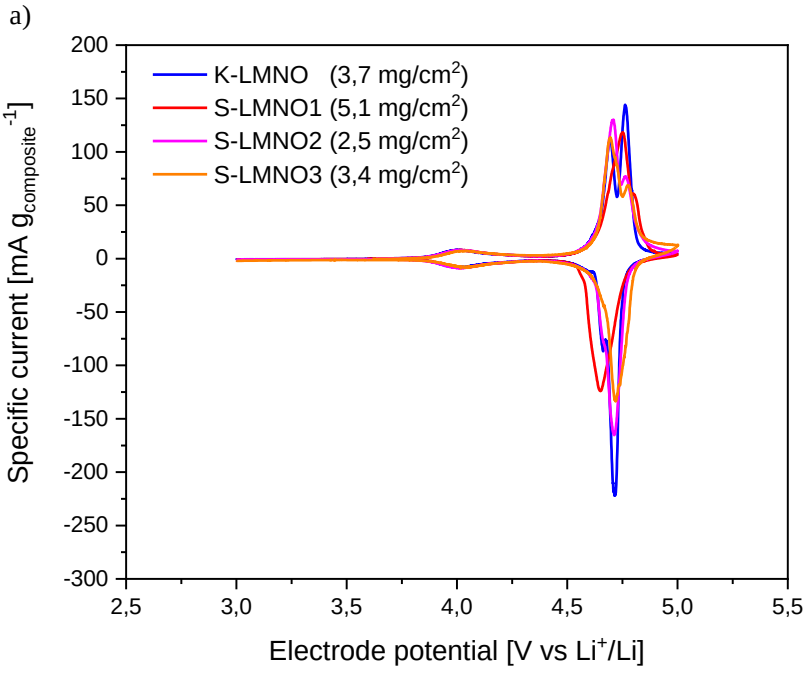

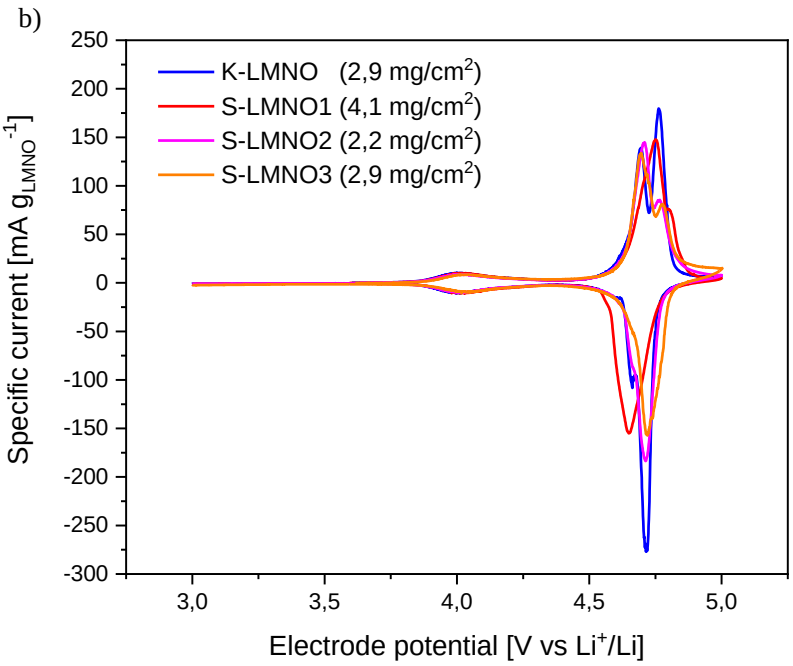

Figure 60 – Comparison of the second voltammogram cycle of the K-LMNO, S-LMNO1, S-LMNO2 and S-LMNO3 cathodes with the specific current normalized to a) the composite mass and b) the LMNO mass.

Figure 61 shows the discharge curve normalized to the LMNO mass of the 2nd charge-discharge cycle performed at C/10 for each formulation tested, and Figure 62 the relative differential capacity profile vs electrode potential. There are no visible differences on the characteristic plateau of LMNO-based cathodes for the redox couples. This is highlighted by the differential analysis of the profiles reported in Figure 62. The only difference is in the delivered capacity which follow the order S-LMNO1 (126 mAh/g_{LMNO}) > K-LMNO (121 mAh/g_{LMNO}) > S-LMNO2 (114 mAh/g_{LMNO}) ≥ S-LMNO3 (113 mAh/g_{LMNO}). The capacity order for K-LMNO and S-LMNO1 is reversed compared to the CV results because, as stated above, the CVs were collected during a conditioning phase.

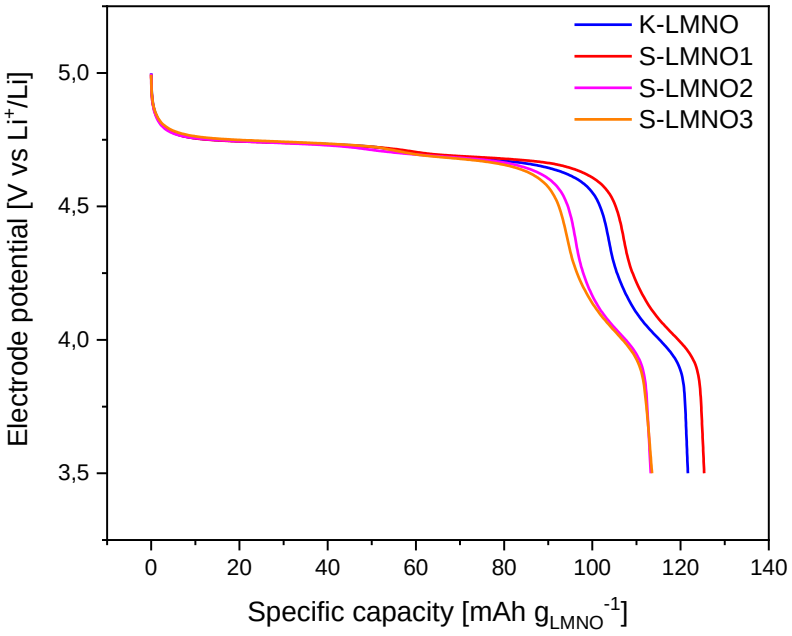

Figure 61 – Comparison of the discharge curve normalized to the LMNO mass of the 2nd GCPL cycle at C/10 of the K-LMNO, S-LMNO1, S-LMNO2, and S-LMNO3 cathodes.

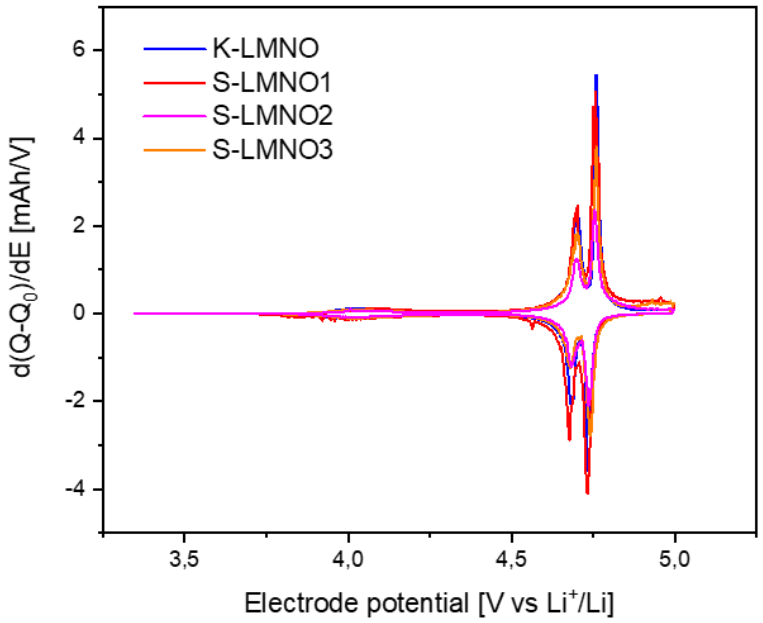

Figure 62 – Comparison of the differential capacity of the 2nd GCPL cycle at C/10 of the K-LMNO, S-LMNO1, S-LMNO2, and S-LMNO3 cathodes.

Figure 63 and Figure 64 show the comparison of composite specific capacity and coulombic efficiency at each C-rate adopted during the galvanostatic rate capability test. Both the formulations that featured 80% of LMNO and 10% of carbon delivered the highest specific capacity but S-LMNO1 with Solef PVDF showed a slightly higher coulombic efficiency respect the K-LMNO with Kynar PVDF. In addition, S-LMNO1 response is extremely interesting if we consider the high mass loading of this electrode. In turn, despite the voltammetric trends observed above, both S-LMNO2 and S-LMNO3, that feature 5% and 7.5% of carbon, respectively, have a lower capacity retention at the highest currents. At C/1 they feature 30% lower specific capacity than K-LMNO and S-LMNO1, which is not compensated by the increase of active materials in the composite formulation (10-5%). So, we can observe that trying to use more active material while reducing the carbon additive (below 10%) and binder is not satisfactory solution for LMNO-based cathodes.

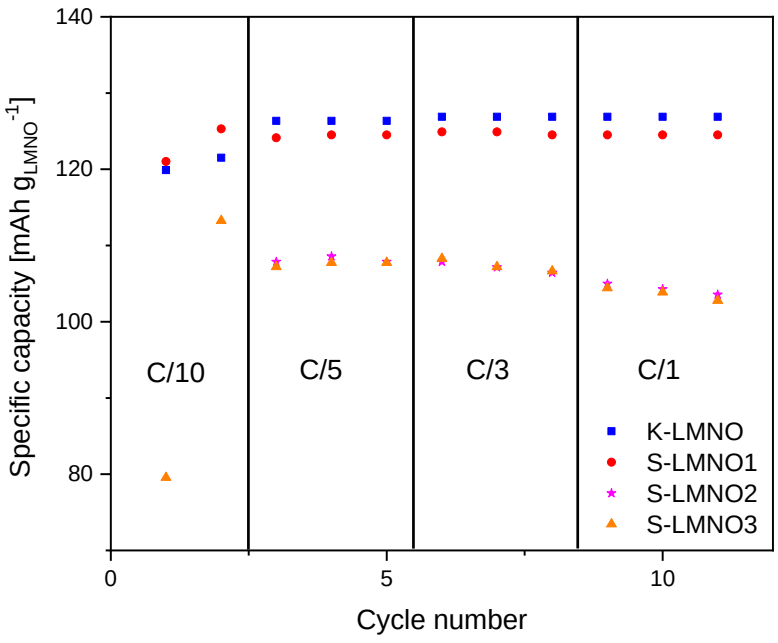

Figure 63 – Comparison of capacity retention of K-LMNO, S-LMNO1, S-LMNO2 and S-LMNO3 as a function of composite capacity delivered at different C-rates with cut-off potentials 3.5 - 5 V vs Li^+/Li.

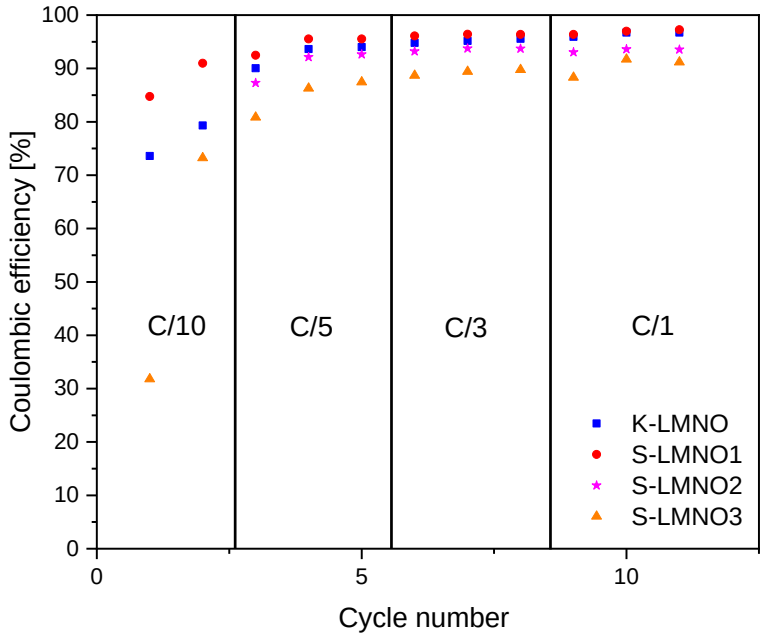

Figure 64 - Comparison of coulombic efficiency of K-LMNO, S-LMNO1, S-LMNO2 and S-LMNO3 delivered at different C-rates with cut-off potentials 3.5 - 5 V vs Li^+/Li.

Figure 65 compares the composite specific capacity delivered in repeated charge-discharge cycles at C/1. Even if the K-LMNO cathode reached only 70 cycles, we can say that S-LMNO1 cathode showed the best performance in life stability, losing 23% of the initial capacity. This indicates that the binder content should not be lowered below 10%.

Note that we used a protocol that can be considered as an "accelerated test" performed to have results within my internship period. Indeed, cycling stability is expected to ameliorate by charging the electrode a lower rate (e.g., C/5), which can also be beneficial for a safe operation of the metallic lithium that we adopted as counter electrode in our half-cells.

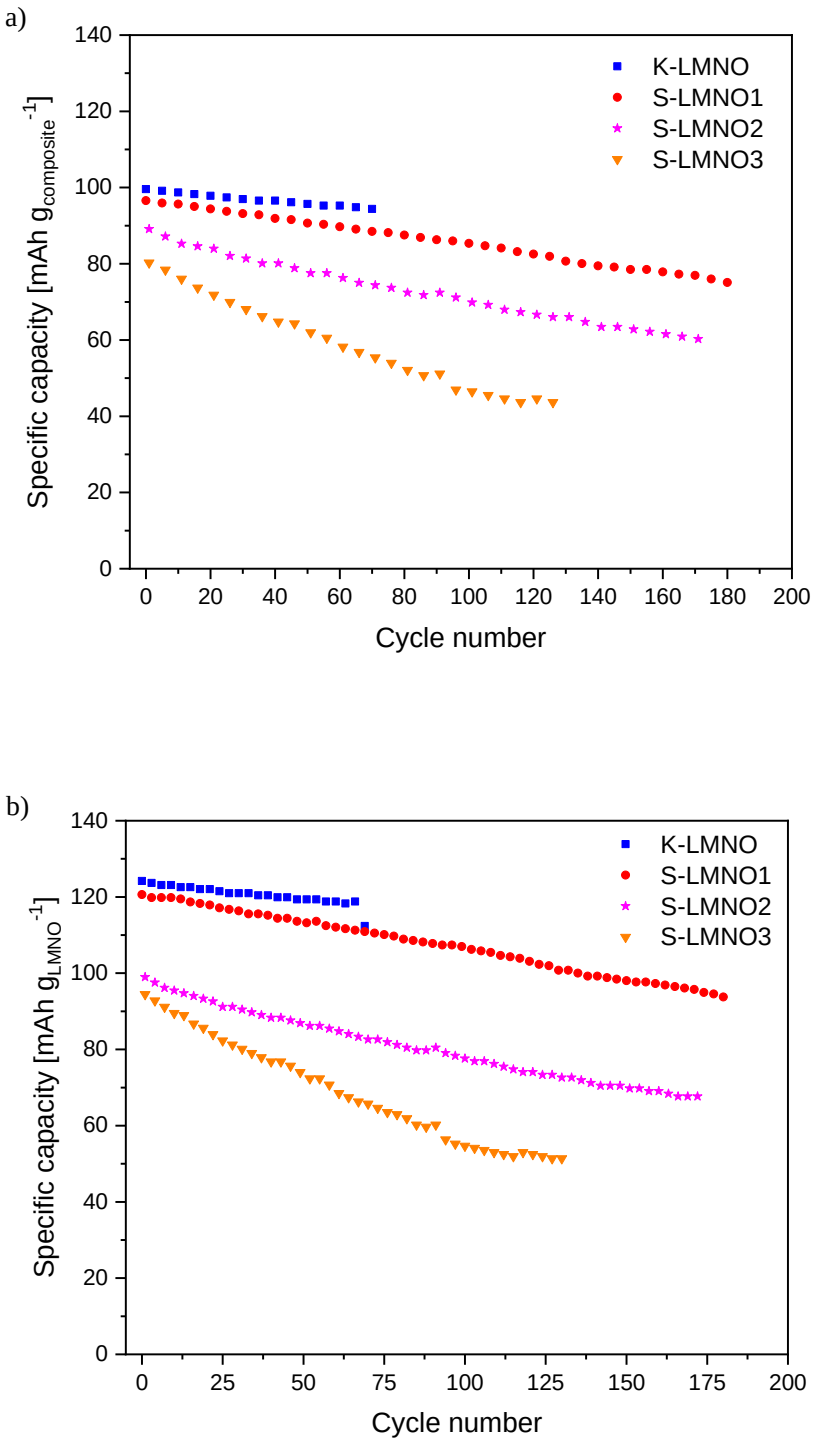

Figure 65 – Comparison of the stability test at C/1 for K-LMNO, S-LMNO1, S-LMNO2, and S-LMNO3 as a function of a) the composite specific capacity and b) the LMNO specific capacity with cut-off potentials 3.5 - 5 V vs Li^+/Li.

Overall, we can say that LMNO-based cathode proved to have a good rate capability ad different C-rates but suffer from repeated, accelerated cycles at C/1. We can conclude that in this study the best

composition for LMNO is 80-10-10, even with different binders, that showed the best performance. While the other two formulations, with a higher content of active material proved to have poorer performance.

4. Conclusions and outlook

Overall, this work has demonstrated the feasibility of the use of Cobalt-free, LMNO for the development of next-generation, high-voltage Lithium-ion batteries operating beyond 4 V. In addition, it demonstrates that the definition of cathode manufacturing process is extremely important because it greatly affects cathode operation.

Indeed, I evaluated the electrochemical response of LMNO cathodes formulated with different PVDF binder source and different compositions in terms of LMNO, binder and carbon conductive additive mass ratios. All the LMNO-based cathodes performed quite efficiently, especially in the rate capability tests performed. As most of the cathodes, switching from lower to higher discharge current, demonstrated to offer almost the same capacity with only a small loss of capacity for certain cathodes. We observed that the composition and the thickness of the electrodes are extremely important in the electrochemical performance. Trying to reduce the amount of binder and conductive carbon seems to be a valuable choice for electrochemical properties, since more active material is present. However, reducing the binder content leads to manufacturing issues, like detachment of the slurry from the current collector during the pressing process. Furthermore, during disassembling the cell that featured the lower binder content, we noted that most of the composite detached from the current collector and deposited onto the separator. Moreover, as known from literature, electrodes that are too thick can perform poorly as it is more difficult for lithium ions to intercalate in the innermost structure. But the best performing electrode in this study was the thicker one, so for further consideration more research is needed.

Specifically, the experimental work demonstrated that both rate response and cycling stability (under accelerated conditions) are promoted by using the 80% LMNO, 10% PVDF (Kynar or Solef), 10% carbon composition with a composite mass loading as high as 5 mg/cm^2. The best electrodes featured up to 125 mAh g^{-1} at C/10 (corresponding to the nominal value), a constant capacity retention at different discharge rates (C/5, C/3 and C/1) and a capacity fade of 23% after 180 cycles at C/1.

Overall, this thesis provides useful guidelines for future research. Indeed, it suggests good practices for LMNO cathode preparation, that will be further exploited under the PNRR Project CNMS-Spoke 13-MOST (Code: CN00000023) and eventually by MIDAC SpA for the development of novel active materials and manufacturing processes for next generation, high voltage lithium- ion batteries. The electrochemical results can be taken as a benchmark for the comparison of the new cathodes that will be developed and/or for the novel electrolytes that will be formulated to improve cycling performance. Indeed, LMNO-based cathodes work at high potentials but suffer from different points. This material suffers from undesirable cathode-electrolyte reactions, which results in electrolyte

decomposition, transition-metal ion migration (specially manganese), surface corrosion and dissolution in the cathode. For those reasons more research is needed in the field of surface treatments of cathodes and in new electrolytes that are more stable at high voltages for improving the performance of LMNO-based cathodes to go through their commercialization.

Acknowledgments

This work has been carried at the Laboratory of Electrochemistry of Materials for Energetic (LEME) of the Department of Chemistry "Giacomo Ciamician" of the University of Bologna. It has been developed under the collaborative project set between MIDAC S.p.A., partner of the IPCEI/012/00B2 program (CUP: B22C22000090008) and GISEL – INSTM, Consorzio Interuniversitario Nazionale per la Scienza e Tecnologia dei Materiali (Research unit: UNIBO), and within the PNRR Project CNMS-Spoke 13-MOST (Code: CN00000023).

I want to thank Professor Francesca Soavi for availability, trust and help given to me in those recent months of work. Also, Dr. Antunes Staffolani for helping in writing this thesis work. Dr. Daniele Marchese and Ing. Matteo Cavalletti from MIDAC S.p.A. for developing the thesis study and giving us the materials needed for the research.

A special thanks to Alessandro Gregucci and the guys from LEME of the Department of Chemistry "Giacomo Ciamician" for helping me in the laboratory work, for the explanation of all my questions and for the nice environment in the workplace during those months.

Thanks to my family, in particularly my parents Luciano and Cristina for everything they did for me, to Michela and my friends that supported me in all those years of study and exams.

References

[1] Intergovernmental Panel on Climate Change (IPCC), “Climate Change 2021 - The Physical Science Basis,” 2021.

[2] Climate.gov, 23 June 2022. [Online]. Available: https://www.climate.gov.

[3] Wikipedia, “Accordo di Parigi (2015),” [Online].

[4] B. Petroleum, “Energy Outlook 2022”.

[5] H. Ritchie, M. Roser and P. Rosado, “CO_2 and Greenhouse Gas Emissions,” 2020.

[6] Olanrewaju, M. J. B. Kabeyi and O. Akanni, “Sustainable Energy Transition for Renewable and Low Carbon Grid Electricity Generation and Supply,” *Frontiers in Energy Research,* 2022.

[7] D. Popp, “Deal confirms zero-emissions target for new cars and vans in 2035,” 2022. [Online]. Available: https://www.europarl.europa.eu/news.

[8] F. Marchesini, “Water processable polymers for high voltage cathodes in next generation,” 2021.

[9] M. S. Guney and Y. Tepe, “Classification and assessment of energy storage systems,” *ELSEVIER,* 2016.

[10] B. B. Adetokun, O. Oghorada and S. J. Abubakar, “Superconducting magnetic energy storage systems: Prospects and challenges for renewable energy applications,” *ELSEVIER,* 2022.

[11] J. Lindorfer, D. C. Rosenfeld and H. Böhm, “Fuel Cells: Energy Conversion Technology,” 2020.

[12] X. Luo, J. Wang, M. Dooner and J. Clarke, “Overview of current development in electrical energy storage technologies and the application potential in power system operation,” *Applied Energy,* 2015.

[13] M. E. Şahin, F. Blaabjerg and A. Sangwongwanich, “A Comprehensive Review on Supercapacitor Applications and Developments,” *Energies,* 2022.

[14] A. Z. Weber, M. M. Mench, J. P. Meyers, P. N. Ross, J. T. Gostick and Q. Liu, “Redox flow batteries: a review,” *Journal of Applied Electrochemistry,* 2011.

[15] E. Sanchez-Díez, E. Ventosa, M. Guarnieri, A. Trovò, C. Flox, R. Marcilla, F. Soavi, P. Mazur, E. Aranzabe and R. Ferret, “Redox flow batteries: Status and perspective towards sustainable stationary energy storage,” *ELSEVIER,* 2020.

[16] C. Pillot, “The Rechargeable Battery Market and Main Trends 2018-2030,” 2019.

[17] I. E. Agency, “Global EV Outlook 2020: Entering the decade of electric drive?,” 2020.

[18] C. Julien, A. Mauger, A. Vijh and K. Zaghib, Lithium Batteries - Science and Technology.

[19] C. Schultz, S. Vedder, M. Winter and S. Nowak, "Investigation of the decomposition of organic solvent-based lithium ion battery electrolytes with liquid chromatography-mass spectrometry," 2016.

[20] D. Aurbach, E. Zinigrad, Y. Cohen and H. Teller, "A short review of failure mechanisms of lithium metal and lithiated graphite anodes in liquid electrolyte solutions".

[21] C. P. Sandhya, B. John and C. Gouri, "Lithium titanate as anode material for lithium-ion cells: a review," 2014.

[22] X.-B. Cheng, R. Zhang, C.-Z. Zhao and Q. Zhang, "Toward Safe Lithium Metal Anode in Rechargeable Batteries: A Review," *American Chemical Society,* 2017.

[23] F. Wu, J. Maier and Y. Yu, "Guidelines and trends for next-generation rechargeable lithium and lithium-ion batteries," *Chemical Society Reviews,* 2020.

[24] D. Fabiani, Tecnologie Elettriche Innovative, 2019.

[25] R. Hausbrand, G. Cherkashinin, H. Ehrenberg, M. Gröting, K. Albe, C. Hess and W. Jaegermann, "Fundamental degradation mechanisms of layered oxide Li-ion battery cathode materials: Methodology, insights and novel approaches," *Materials Science & Engineering,* 2014.

[26] Noguchi, M. Yoshio and Hideyuki, "A Review of Positive Electrode Materials for Lithium-Ion Batteries," 2009.

[27] Y. Lyu, X. Wu, K. Wang, Z. Feng, T. Cheng, Y. Liu, M. Wang, R. Chen, L. Xu, J. Zhou, Y. Lu and B. Guo, "An Overview on the Advances of LiCoO2 Cathodes for Lithium-Ion Batteries," *Advanced Energy Materials,* 2021.

[28] H. Xia, Z. Luo and J. Xie, "Nanostructured LiMn2O4 and their composites as high-performance cathodes for lithium-ion batteries," *Progress in Natural Science: Materials International,* 2012.

[29] M. Bianchini, M. Roca-Ayats, P. Hartmann, T. Brezesinski and J. Janek, "There and back again - The journey of LiNiO2 as cathode active material".

[30] B. Ramasubramanian, S. Sundarrajan, V. Chellappan, M. V. Reddy, S. Ramakrishna and K. Zaghib, "Recent Development in Carbon-LiFePO4 Cathodes for Lithium-Ion Batteries: A Mini Review," 2022.

[31] J. Xiang, Y. Wei, Y. Zhong, Y. Yang, H. Cheng, L. Yuan, H. Xu and Y. Huang, "Building Practical High-Voltage Cathode Materials for Lithium-Ion Batteries," *Advanced Materials.*

[32] H. Zhao, W.-Y. A. Lam, L. Sheng, L. Wang, P. Bai, Y. Yang, D. Ren, H. Xu and X. He, "Cobalt-Free Cathode Materials: Families and their Prospects," *Advanced Energy Materials,* 2022.

[33] F. Zou and A. Manthiram, “A Review of the Design of Advanced Binders for High-Performance Batteries,” *Advanced Energy Materials,* 2020.

[34] B. European Commission, “https://eur-lex.europa.eu,” 2019. [Online].

[35] A. Brilloni, F. Marchesini, F. Poli, E. Petri and F. Soavi, “Performance Comparison of LMNO Cathodes Produced with Pullulan or PEDOT:PSS Water-Processable Binders,” *energies,* 2022.

[36] Manthiram, F. Zou and Arumugam, “A Review of the Design of Advanced Binders for High Performance Batteries,” *Advanced Energy Materials,* 2020.

[37] R. Wagner-Wenz, A.-J. v. Zuilichem, L. Göllner-Völker, K. Berberich, A. Weidenkaff and L. Schebek, “Recycling routes of lithium-ion batteries: A critical review of the development status, the process performance, and life-cycle environmental impacts,” *MRS Energy & Sustainability,* 2022.

[38] M. Chen, X. Ma, B. Chen, R. Arsenault, P. Karlson, N. Simon and Y. Wang, “Recycling End-of-Life Electric Vehicle Lithium-Ion Batteries,” *Joule,* 2019.

[39] B. Makuza, Q. Tian, X. Guo, K. Chattopadhyay and D. Yu, “Pyrometallurgical options for recycling spent lithium-ion batteries: A comprehensive review,” *Journal of Power Sources,* 2021.

[40] Y. Yao, M. Zhu, Z. Zhao, B. Tong, Y. Fan and Z. Hua, “Hydrometallurgical Processes for Recycling Spent Lithium-Ion Batteries: A Critical Review,” *ACS Sustainable Chemistry & Engineering,* 2018.

[41] S. Li, S. Tsutsumi, S. Shironita and M. Umeda, “Peak Attribution of the Differential Capacity Profile of a LiCoO2-based Three-electrode Li-ion Laminate Cell,” *The Electrochemical Society of Japan,* 2021.

[42] A. Ursua, L. M. Gandia and P. Sanchis, “Hydrogen Production From Water Electrolysis: Current Status and Future Trends,” *IEEE,* 2011.

[43] D. Linden and T. B. Reddy, Handbook of Batteries, third edition.